ACS NANO

ARTICLE

Live Imaging of Label-Free Graphene Oxide Reveals Critical Factors Causing Oxidative-Stress-Mediated Cellular Responses

Sandra Vranic,[†,‡,#] Artur Filipe Rodrigues,[†,‡,#] Maurizio Buggio,[†,‡] Leon Newman,[†,‡] Michael R. H. White,[§] David G. Spiller,[∥] Cyrill Bussy,*[,†,‡] and Kostas Kostarelos*[,†,‡]

†Nanomedicine Lab, Faculty of Biology, Medicine and Health, The University of Manchester, AV Hill Building, Manchester M13 9PT, U.K.

‡National Graphene Institute, The University of Manchester, Booth Street East, Manchester M13 9PL, U.K.

§School of Biological Sciences, Faculty of Biology, Medicine and Health, The University of Manchester, Michael Smith Building, Manchester M13 9PT, U.K.

∥FBMH Platform Sciences, Enabling Technologies & Infrastructure, FBMH Research & Innovation, Faculty of Biology, Medicine and Health, The University of Manchester, Michael Smith Building, Manchester M13 9PT, U.K.

Ⓢ Supporting Information

ABSTRACT: The interest in graphene and its translation into commercial products has been expanding at a high pace. Based on previously described pulmonary safety concerns for carbon nanomaterials, there is a great need to define parameters guiding interactions between graphene-based materials and the pulmonary system. The aim of the present study was to determine the importance of two critical parameters: lateral dimensions of the material and coating with proteins in relation to each other and their pulmonary impact. Endotoxin-free materials with distinct lateral dimensions, s-GO (50−200 nm) and l-GO (5−15 μm), were produced and thoroughly characterized. Exploiting intrinsic fluorescence of graphene oxide (GO) and using confocal live-cell imaging, the behavior of the cells in response to the material was visualized in real time. Although BEAS-2B cells internalized GO efficiently, l-GO was linked to higher plasma membrane interactions correlated with elevated reactive oxygen species (ROS) levels, pro-inflammatory response, and greater cytotoxicity, in agreement with the oxidative stress paradigm. For both GO types, the presence of serum alleviated lipid peroxidation of plasma membrane and decreased intracellular ROS levels. However, protein coating was not enough to entirely mitigate toxicity and inflammatory response induced by l-GO. *In vitro* results were validated *in vivo*, as l-GO was more prone to induce pulmonary granulomatous response in mice compared to s-GO. In conclusion, the lateral dimension of GO played a more important role than serum protein coating in determining biological responses to the material. It was also demonstrated that time-lapse imaging of live cells interacting with label-free GO sheets can be used as a tool to assess GO-induced cytotoxicity.

KEYWORDS: 2D materials, graphene, confocal live-cell imaging, inflammation, lungs, nanotoxicology
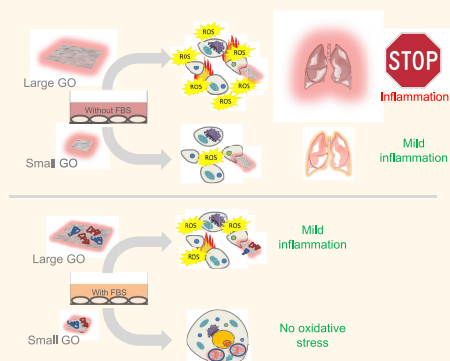
The interest in graphene and its translation into commercial products have been expanding during the past few years. Graphene-based materials (GBMs) are a large family of different materials[1,2] varying tremendously in their lateral dimensions, number of carbon layers (*i.e.*, thickness), and surface properties. Today, GBMs are already contained in various commercial products (sportswear, tennis rackets, bicycle frames, tires, or innovative paints), while conductive inks, paints, or filaments for 3D printing are expected to become components of flexible displays and wearable electronics in the near future.[3] Longer-term applications are also anticipated in the healthcare sector, either as drug delivery systems, as biosensors for health monitoring

and e-health, or in the form of biomedical implants.[2] However, in order to be fully adopted by both industry and society, new enabling technologies need to demonstrate not only their benefits but also their long-term safety and sustainability.[2,4]

In consideration of the previously described pulmonary health and safety concerns for carbon nanomaterials (*e.g.*, carbon nanotubes)[5,6] and the fact that the lungs will be one of the primarily exposed organs following inhalation of nanoma-
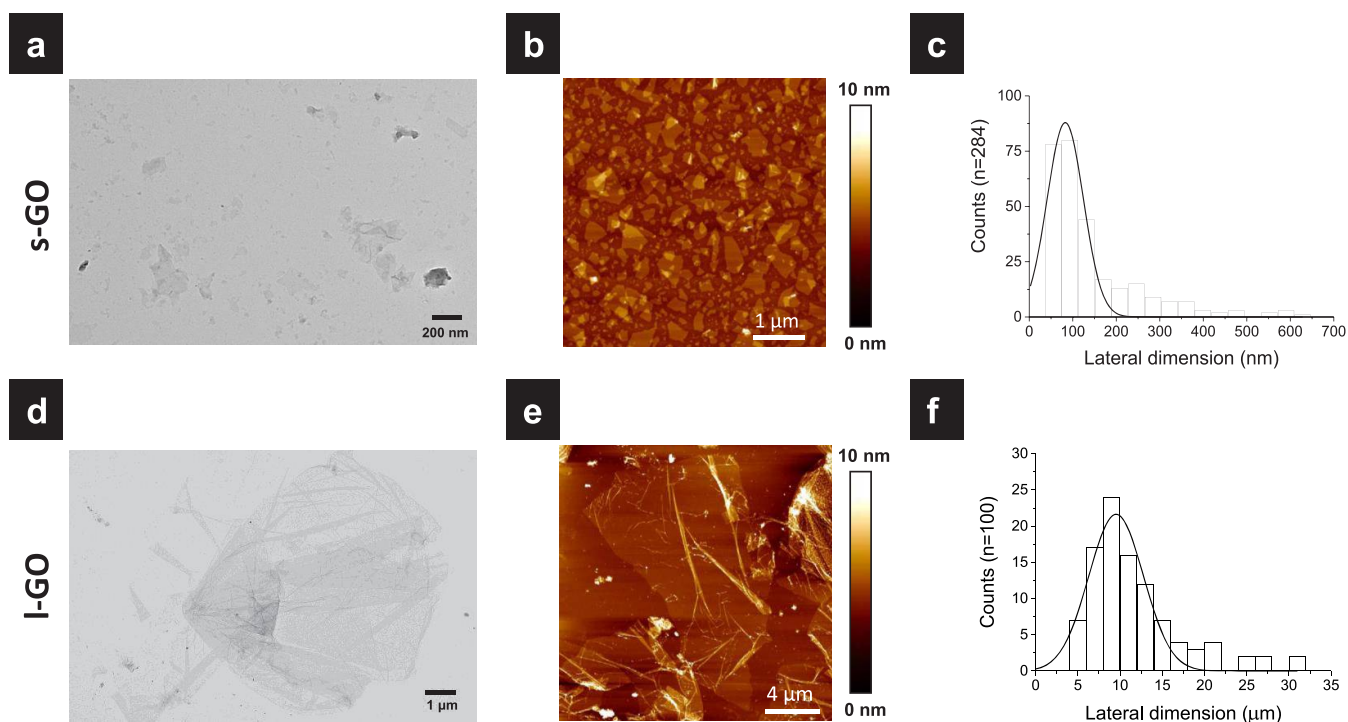
Figure 1. Physicochemical characterization of s-GO (a–c) and l-GO (d–f). (a) TEM micrograph of s-GO. (b) AFM height image of s-GO. (c) Lateral dimension distribution analysis for s-GO. (d) TEM micrograph of l-GO. (e) AFM height image of l-GO. (f) Lateral dimension distribution analysis for l-GO.

terials (in particular airborne GBMs), there is a great need to understand the critical parameters impacting interactions between GBMs and the cells of the pulmonary system.

For the vast majority of GBMs, interactions with mammalian cells and their overall safety profile remain largely unknown. By far the most studied type of GBMs in biological research has been graphene oxide (GO), the heavily oxidized form of graphene in the form of sheets. This popularity can be explained by its ease of production and its hydrophilic surface character that allows its colloidal dispersion in the aqueous and physiological milieu.

Hazard assessment studies have indicated that structure–function relationships should be based on specific physicochemical properties of the studied nanomaterial. Both intrinsic (e.g., physicochemical properties) and acquired (e.g., aggregation state in local milieu or secondary coating with components from the cell culture medium, blood, or different organs) features need to be taken into consideration before obtaining a clear understanding of the parameters that could lead to adverse effects.[7] In addition, the oxidative stress paradigm has been shown to successfully explain and predict the outcomes of the cellular response to many nanomaterials.[8−10] According to this paradigm, cellular response to nanomaterials is governed by induction of oxidative stress, which can either be counterbalanced by the activity of antioxidative enzymes (tier 1 response), lead to subsequent activation of pro-inflammatory pathways (tier 2 response), or result in cell death in the case of excessive levels of reactive oxygen species (ROS) production (tier 3 response).

Previous in vitro studies have compared graphene oxide sheets of large (2 μm) and small (350 nm) lateral dimensions to conclude that larger materials were more inflammogenic than smaller ones, with an almost flat inflammatory response for the small GO even at the highest concentration (6 μg/mL)

tested.[11] A different study by Ma et al. reported that large GO (750−1300 nm) induced more cytokine production than two smaller GO types (50−350 or 350−750 nm), but concluded that all GOs were inflammogenic.[12] GO sheets were also found to be pro-fibrotic in cells and animals, with larger GO (1676 nm) sheets being more potent than their smaller counterparts (179 nm).[5] Currently, only a limited number of studies have reported that small GOs may cause more damage than larger GO (above 1 μm). Orecchioni et al. found smaller GOs (<1 μm) to be more inflammogenic than large GOs (1−10 μm), even though large GOs was still inducing elevated levels of a subset of cytokines.[13] In relation to surface coating, different studies have demonstrated that bovine serum albumin[14−16] or the level of serum in the cell culture medium[17,18] could greatly alleviate the toxic response observed without coating, suggesting that the shielding effect of adsorbed proteins was able to mitigate adverse responses to materials. In most cases, however, the two parameters of lateral dimensions and serum protein coating were considered separately, which precluded any analysis of their interrelation and did not allow determination of the importance that each parameter holds in the context of cellular response induced by GOs. Moreover, the effect of protein coating on the effect of micrometer-sized GO sheets (>3 μm) is not well documented, as most studies have only considered GO nanosheets (<500 nm).

In the present study, we aimed to comparatively determine the importance of these two parameters (i.e., lateral dimensions and serum protein surface coating) in relation to induction of oxidative stress, inflammation, and cytotoxicity in a human lung epithelial cell line (BEAS-2B). On the basis of previous reports describing the individual role of each criterion, we postulated that while surface adsorption of proteins may alleviate the adverse effects induced by smaller GO sheets, by shielding their most reactive parts, it may not be sufficient for larger materials.

Therefore, we also hypothesized that lateral dimensions may have a more dominant role than protein shielding on the biological impact of the GO.[19] In addition, based on the results obtained with various nanomaterials, we wanted to test whether cellular responses to GOs can be explained and predicted using the oxidative stress paradigm.[10]

To address these questions, we produced endotoxin-free materials with two clearly distinct lateral dimensions—small, nanometer-sized GO (50−200 nm; s-GO) and large, micrometer-sized GO (5−15 μm; l-GO)—using a modified Hummers method.[20] We demonstrated that these two materials differed only by their lateral dimensions, allowing us to determine the role of one physicochemical parameter at a time. The role of serum protein coating in the initial phase of the interaction between nanomaterials and cells was addressed by controlling the presence of fetal bovine serum (FBS) (10%) during the first 4 h of exposure. Exploiting the intrinsic fluorescence of the two GOs without introducing additional surface modifications and/or without attaching fluorescent dyes, we were able to follow in real time the interactions of GOs with cells at a single-cell level over a 24 h period using confocal live-cell imaging. Furthermore, correlation between the lateral dimensionality and serum coating of the material with cytotoxicity, induction of oxidative stress, and inflammation was attempted.

RESULTS AND DISCUSSION

Preparation and Characterization of s-GO and l-GO. To address the importance of lateral dimensions in cellular responses, we produced two types of GO, differing only in lateral dimensions. Using the previously reported modified Hummers' method optimized to produce the samples in endotoxin-free conditions,[20,21] GOs with small (nanometer-sized) and large (micrometer-sized) lateral dimensions (s-GO and l-GO, respectively) were produced from the same starting graphite powder (Sigma-Aldrich, UK). The two resulting endotoxin-free, water-based dispersions of GO had good colloidal stability at room temperature for at least 6 months.[22]

To confirm the difference in lateral dimensions and the similarities in surface chemistry, a thorough physicochemical characterization was performed. Analyses related to lateral dimensions are presented in Figure 1 (further physicochemical features are summarized in Table 1 and fully reported in Figures S1 and S2). The morphology of the s-GO and l-GO was studied using transmission electron microscopy (TEM) and atomic force microscopy (AFM) (Figure 1a, b, d, and e) as well as optical microscopy (Figure S2a). The size distribution analysis showed that lateral dimensions of the majority of s-GO ranged from 50 to 200 nm (Figure 1c), while l-GO ranged from 5 to 15 μm (Figure 1f). In addition, AFM showed that the average thickness for both materials was approximately 1−2 nm (Figure S1a), indicating that both GO samples were mainly composed of monolayer sheets. These data confirmed that we had successfully prepared two samples of single-layered GOs with lateral dimensions that differ by at least 1 order of magnitude.

Synthesis and the sample preparation process did not change any physicochemical properties other than lateral dimensions; this was confirmed using a detailed physicochemical characterization of the two GO samples (Figures S1 and S2). Optical properties of the two materials were studied by UV−vis and fluorescence spectroscopies (Figures S1b−e and S2b−e). Raman spectroscopy and laser Doppler electrophoresis

Table 1. Physicochemical Characterization of s-GO and l-GO Used in the Present Study

parameter	technique	s-GO	l-GO
lateral dimension[a]	optical microscopy		2−33 μm
	AFM	0.055−0.7 μm	1−20 μm
	TEM	0.1 μm − 1 μm	1−20 μm
thickness	AFM	1.3 ± 0.7 nm	1 nm (1 layer)
optical properties	absorbance	$A_{230} = 0.043 \times C_{GO}$ (μg/mL)	$A_{230} = 0.042 \times C_{GO}$ (μg/mL)
	fluorescence (λ_{exc} 525 nm)	$A_{600} = 0.854 \times C_{GO}$ (μg/mL)	$A_{596} = 1.031 \times C_{GO}$ (μg/mL)
degree of defects (I_D/I_G)	Raman	1.39 ± 0.03	1.32 ± 0.02
surface charge	ζ-potential	−57.1 ± 0.7 mV	−51.7 ± 1.0 mV
functionalization degree	TGA	45%	43%
chemical composition (purity)	XPS	C: 68.8%, O: 30.7%, S: 0.5% (99.5%)	C: 68.8%, O: 30.7%, S: 0.5% (99.5%)
C:O ratio	XPS	2.2	2.2
π−π*, O=C−O, C=O, C−O, C−C, and C=C	XPS	0.2%, 4.7%, 5.0%, 46.5%, 43.6%	0.3%, 5.1%, 5.2%, 45.2%, 44.2%

[a]Lateral dimensions of s-GO and l-GO are reported as a range between the minimum and the maximum size detected.

(measuring zeta-potential) were used to assess the crystallinity and the surface properties of the GOs, respectively. The Raman spectroscopic analysis revealed two bands at 1319 and 1596 cm^{-1}, which are the characteristic D and G bands for most polyaromatic hydrocarbons (Figures S1f and S2f).[23] The D to G band intensity ratio (I_D/I_G) corresponding to the metric of disorder in the graphitic lattice was calculated to be about 1.3 for both materials. Surface charge was analyzed by zeta-potential measurement. Figures S1g and S2g show that the two GO samples were similarly negatively charged when diluted in Milli-Q water. The surface charge measured with a ZetaSizer instrument showed zeta-potential values between −50 and −58 mV at pH 7 and 20 °C. To identify the degree of surface functionalization and to quantify the purity of the GOs as well as the C/O elemental ratio, both thermogravimetric analysis (TGA) and X-ray photoelectron spectroscopy (XPS) were performed (Figures S1h,i and S2h,i). In addition, XPS high-resolution C 1s spectra were recorded to determine the contribution of individual functional groups such as carboxylic, carbonyl, epoxide, or hydroxy (Figures S1i and S2i). Results showed similar surface chemistry profiles for both s-GO and l-GO (Table 1). Taken together, the analysis demonstrated that both s-GO and l-GO showed comparable physicochemical and structural properties with the exception of desired disparity in lateral dimensions.

Interactions of s-GO and l-GO with BEAS-2B Cells and Cytotoxicity. Inhalation is considered to be one of the main routes of exposure in nanomaterial manufacturing, occupational settings, or following the wear-and-tear aging of nanomaterial-enabled/surface-coated consumer products. For potential biomedical applications of GO aiming to deliver pharmaceuticals or imaging agents or in the development of novel therapeutic strategies (e.g., photothermal therapy) in the lungs,[2,24] it is equally important to reveal the full toxicological profile of these materials and understand their biological responses at a cellular level. Therefore, we selected the BEAS-2B human immortalized bronchial epithelial cell line as a

pulmonary model to assess the cell responses to s-GO and l-GO exposure.

GOs are commonly known to be well-dispersed in water, allowing the visualization of isolated sheets of a single-layer thickness using TEM and AFM (Figure 1).[13,20] However, as soon as these highly functionalized (carboxyl, epoxy, and hydroxy) materials are introduced into saline solution such as cell culture media, their colloidal stability may alter, resulting in agglomeration due to physical instability (Figure S3, left panel, Figure S4, Table S1).[25−27] In contrast, dispersion of the sheets and cell treatment in the presence of FBS not only could improve dispersibility in saline conditions *via* steric shielding but has also been shown to modify the toxicological profile in comparison to FBS-free conditions (Figure S3, right panel, Figure S5, Table S1).[25,28,29] We therefore decided to interrogate whether the presence or absence of FBS during the initial interaction between GOs and the cells (during a "contact period" of 4 h) would influence the biological outcome. Treatment in the absence of FBS during the first 4 h would replicate an exposure scenario in the occupational and general environment, through inhalation of bare materials that would initially adsorb a limited amount of proteins from the lung fluid.[30] On the other hand, using FBS from the beginning of the treatment would reveal whether protein coronation— more relevant in the case of a biomedical application where the materials would be typically injected into the bloodstream— could alleviate or suppress toxicity.[7,19]

To address these questions, we initially observed cellular morphology and interactions of the materials with cells using high-resolution confocal live imaging and optical microscopy. Subsequently, we performed a Trypan Blue dye exclusion assay based on cell counting, a live/dead cell staining (propidium iodide/annexin V assay), and a viability assay (modified LDH assay), after exposing the cells to either s-GO or l-GO for 24 or 72 h in complete medium (10% FBS), following an initial 4 h period in the presence (w/FBS) or absence of 10% FBS (w/o FBS).

Using optical microscopy (Figure S6), we observed that both l-GO and s-GO interacted with the cells in a dose-dependent manner, forming agglomerates on the cell surface regardless of the presence of FBS. At the lowest concentration used, cell morphology did not seem to change upon interacting with either of the two GOs (Figure S6). However, the surface of the tissue culture dish covered by the cell monolayer appeared to be remarkably reduced after l-GO treatment, especially for l-GO w/o FBS in comparison to l-GO w/FBS even at a concentration as low as 1 μg/mL. These gaps in the surface covered by cells were associated with a high number of floating cells under these conditions. In contrast, the impact of s-GO on the cell monolayer appeared significant only at 10 μg/mL s-GO w/o FBS and was completely absent with s-GO w/FBS, irrespective of the concentration used.

As reported in Figures S1d and S2d, both s-GO and l-GO demonstrate intrinsic fluorescent properties that we exploited to better understand the dynamics of cellular interactions with GOs using high-resolution live confocal imaging microscopy. We first performed a thorough characterization of the optical properties of both GOs in cell-free conditions and when dispersed in cell culture medium, using a spectrofluorimeter and a high-resolution confocal laser scanning microscope. The fluorescence emission profile of the materials dispersed in water, created using different excitation wavelengths, revealed that both GOs can be excited in different regions of the

spectrum (Figure S7). Using 594 nm as the excitation wavelength, the maximum emission wavelength was found to range between 620 and 690 nm (Figure S8a). This was confirmed by spectral analysis of the l-GO dispersed in cell culture medium, using a high-resolution confocal laser scanning microscope (Figure S8b). Furthermore, images of both materials dispersed in the cell culture medium in the presence or absence of FBS showed that the intrinsic optical properties of GO can be exploited to observe the materials, using high-resolution confocal microscopy (Figure S8c). Our findings on the intrinsic fluorescent properties of GOs are in agreement with several publications reporting and explaining the origin of fluorescence of these materials in suspension.[11,31,32]

We then used these properties to image, using high-resolution confocal live microscopy, over a 24 h period the interactions of BEAS-2B cells with 50 μg/mL of either l-GO (w/FBS or w/o FBS) or s-GO (w/FBS or w/o FBS) (Figure 2
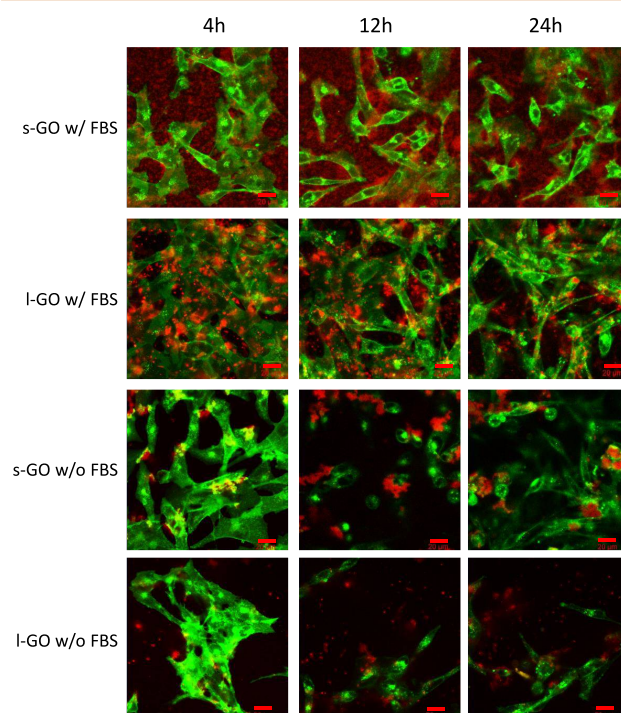

Figure 2. Cellular response to the treatment with s-GO and l-GO in the presence (w/FBS) or absence (w/o FBS) of FBS. Cell confluence, morphology, and mobility were assessed using a high-resolution confocal live imaging microscope, during the treatment of the cells with 50 μg/mL s-GO or l-GO for 24 h in the presence or absence of FBS for the first 4 h. Represented are images of a time lapse taken at indicated time points. Staining of the cells is as follows: Green = cell membrane, red = materials, either s-GO or l-GO.

and Videos S1 to S12). Differences in the dispersibility of the two GOs in cell culture medium and in the presence or absence of FBS were noticeable (Figure S3), indicating that both s-GO and l-GO were better dispersed in the presence of FBS. Using the CellMask green plasma membrane stain to label the cell membranes, we were able to follow cellular motility, proliferation, apoptosis, and confluence (Videos S1 to S12). In agreement with optical microscopy, confocal live imaging revealed that the treatment with l-GO (w/FBS or w/o FBS) led to decreased confluence and increased cellular detachment from the support, compared to treatment with s-GO (w/FBS
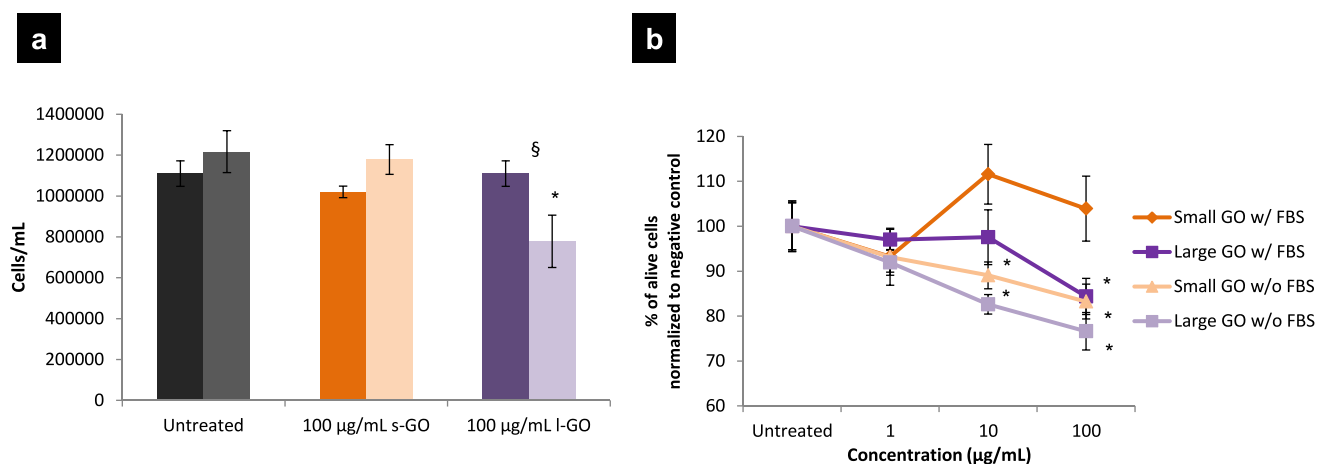
Figure 3. Cytotoxic response to s-GO and l-GO treatment in the presence or absence of FBS. (a) Cell number assessed by counting live cells after 24 h of treatment with 100 μg/mL s-GO or l-GO in the presence or absence of FBS for the first 4 h. Cell count was performed using Trypan Blue exclusion dye. 10% DMSO was used as a positive control (counted cell number = 410 667 $\pm$ 16 441 cells/mL). Results are represented as average cell number $\pm$ SD. Data were statistically analyzed using analysis of variance (one-way ANOVA) with $p < 0.05$ considered as significant. *Statistically different from untreated cells. §Statistically different from the corresponding condition in the presence of FBS. (b) Viability of the BEAS-2B cells was tested after 24 h incubation with either s-GO or l-GO in the presence or absence of FBS. After 4 h of incubation with the material without FBS, cell culture media was completed with 10% FBS. Indirect LDH assay was used. 10% DMSO was used as a positive control (% of live cells normalized to untreated cells = 69% $\pm$ 4%). Results are represented as mean % of live cells $\pm$ SD. Data were statistically analyzed using analysis of variance (one-way ANOVA) with $p < 0.05$ considered as significant. *Statistically different from untreated cells. §Statistically different from the corresponding condition in the presence of FBS.
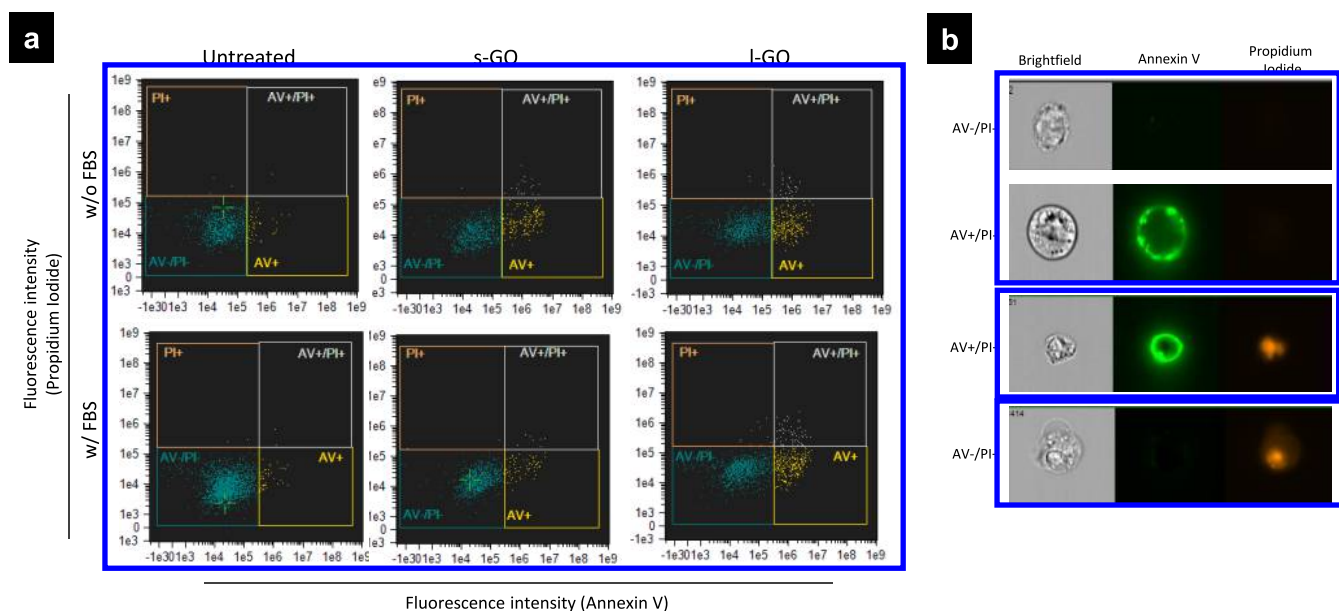

Figure 4. Cytotoxicity of the s-GO and l-GO in the presence or absence of FBS assessed using annexin V/propidium iodide (PI) staining using imaging flow cytometry (Imagestream). (a) Analysis of the cellular death of untreated and cells treated with 50 μg/mL s-GO or l-GO dispersed in the absence of FBS for the first 4 h (w/o FBS) or in the presence of FBS (w/FBS) using annexin V/PI staining. Bivariate plots include intensity of fluorescence collected using channels for annexin V and PI. (b) Representative images of the cells treated with GO, captured by an imaging flow cytometer and previewed in Imaging Gallery. Displayed cells correspond to different gates (AV−/PI−, AV+, AV+/PI+, and PI+) from a bivariate plot (a). First column shows brightfield images of the cells, second column shows fluorescence attributed to annexin V, and third column shows fluorescence attributed to PI.

or w/o FBS) (Figure 2 and Videos S1 to S12). This effect was found to be more pronounced when the treatment was performed without FBS. Time-lapse live-cell microscopy with an overlay of the bright-field channel (cellular morphology) and the red channel (intrinsic GO signal) offered insight into the kinetics of these processes. It showed that already after 2 h of treatment with l-GO w/o FBS, cells started to display changes in their morphology compared to untreated cells (or cells

treated with s-GO w/FBS or w/o FBS), leading to cell death and detachment at 6 h of treatment onward (Videos S3 and S6). The addition of 10% FBS after 4 h of treatment did not alleviate the cytotoxic response following l-GO exposure. It was instead only slightly attenuated with cells continuously detaching from the support (up to 24 h). In comparison, motility and proliferation capacity of untreated cells and cells exposed to s-GO (w/FBS or w/o FBS) were not affected. We
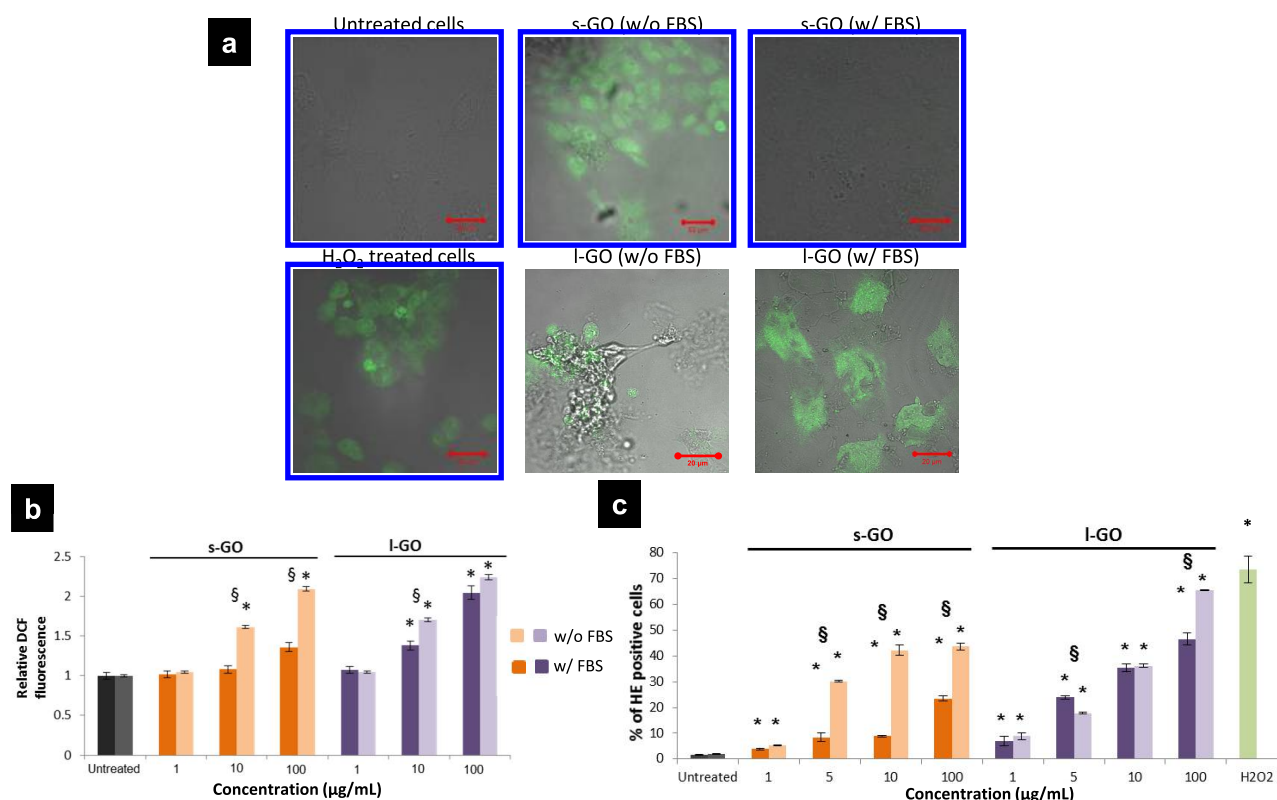
Figure 5. Intracellular ROS production assessed using DCF-DA and HE probes. (a) Intracellular ROS production after treatment with 50 μg/mL s-GO or l-GO for 4 h using DCF-DA probe and confocal live-cell imaging. Scale bars = 20 and 50 μm. (b) Dose escalation study of the intracellular ROS production after treatment with indicated concentrations of the material for 4 h using DCF-DA probe. Results are represented as mean relative fluorescence intensity of the cells $\pm$ SD. Data were statistically analyzed using analysis of variance (one-way ANOVA) with $p < 0.05$ considered significant. *Statistically different from untreated cells, §Statistically different from the corresponding condition in the presence of FBS, $p < 0.05$. (c) Dose escalation study of the intracellular ROS production after treatment with indicated concentrations of the material for 4 h using HE probe. After treatment, supernatants were removed, and cells harvested, centrifuged, and resuspended in PBS containing 1 μM HE probe. After 20 min of incubation with the dye cells were analyzed using a FACS Verse flow cytometer. Results are represented as mean % of HE-positive cells $\pm$ SD. Data were statistically analyzed using analysis of variance (one-way ANOVA) with $p < 0.05$ considered significant. *Statistically different from untreated cells, §Statistically different from the corresponding condition in the presence of FBS, $p < 0.05$.

therefore concluded that the intrinsic optical properties of graphene oxide had been successfully exploited to follow the time course and dynamics of cellular interactions with GOs and that time-lapse live-cell imaging can be used to reveal early signs of cytotoxicity (i.e., cell detachment).

To validate the optical and high-resolution confocal live imaging observations, a Trypan Blue assay was initially used. In agreement with the above data, we observed a statistically significant decrease in the cell number only after 24 h l-GO w/o FBS treatment, whereas no impact on cells from 24 h treatment with l-GO w/FBS, s-GO w/FBS, or s-GO w/o FBS could be observed (Figure 3a). To further probe cell viability and understand the mechanism of the cytotoxic response induced by GOs, a modified LDH assay was performed. This assay has been previously optimized in our laboratory to minimize interference of the assay reagents upon interaction with the tested nanomaterials.[33,34] In the absence of FBS, both s-GO and l-GO treatment induced a statistically significant decrease in the percentage of viable cells starting from 10 μg/mL, compared to untreated cells (Figure 3b). A dose-dependent trend was observed for both materials, but no statistically significant differences between l-GO and s-GO were measured. The percentage of live cells after treatment with l-GO (78%) was however lower in comparison to the treatment with s-GO

(83%). In the presence of FBS, treatment with increasing doses of s-GO did not reveal any difference in percentage of live cells in comparison to untreated cells. The l-GO did however cause a statistically significant decrease in cellular viability at the highest concentration of 100 μg/mL, after 24 h of exposure (Figure 3b); this decrease was more pronounced after 72 h of treatment (Figure S9).

The mechanism of cellular death induced by the GOs was subsequently assessed with the propidium iodide (PI)/annexin V assay. In flow cytometry, the size of GO agglomerates can be similar to the size of a cell and therefore appear as an "unstained event" on the annexin V/PI bivariate plot. Subsequently, this can result in an overestimation of the number of live cells in the sample, which can lead to an inaccurate conclusion regarding the cytotoxicity of the tested compound.[35] In contrast, using imaging flow cytometry, we could distinguish whether each acquired event in the bivariate plot is the result of material agglomeration or a cell and accurately determine toxicity induced by the nanomaterials.[36] In the absence of FBS, both s-GO and l-GO caused more cytotoxicity (Figure 4a and Figure S10) than in the presence of FBS (cell viability reaching 88% for s-GO w/FBS vs 77% for s-GO w/o FBS and 76% for l-GO w/FBS vs 63% for l-GO w/o FBS). Irrespective of the presence of FBS during the contact
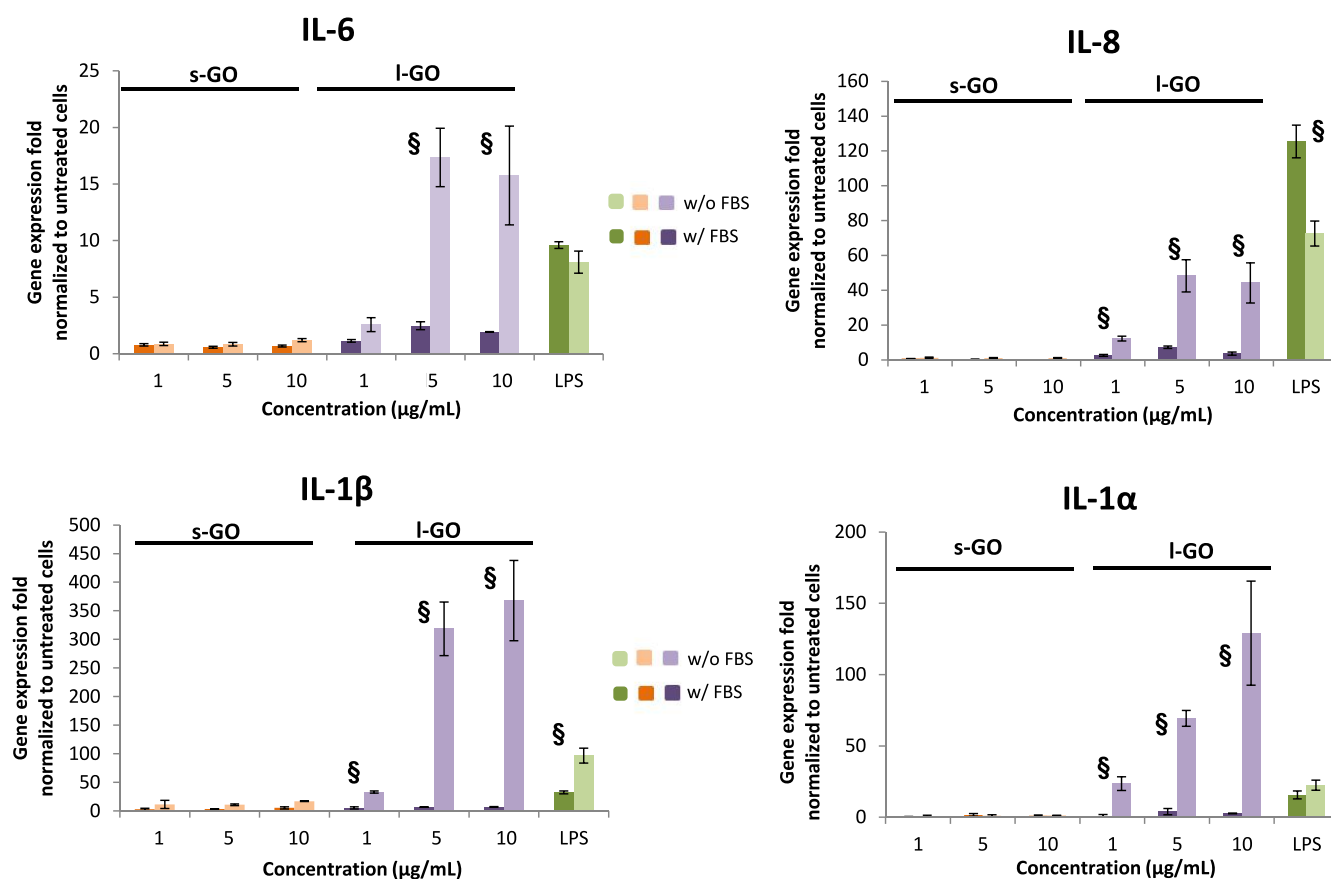
Figure 6. Pro-inflammatory response induced after treatment with s-GO and l-GO for 24 h. Cells were treated with indicated concentrations of s-GO or l-GO in the presence or absence (for the initial 4 h) of FBS over a 24 h period. Gene expression was analyzed using RT-qPCR. Results are represented as gene expression fold increase normalized to untreated cells $\pm$ SD. Data were analyzed by two-way ANOVA. §Statistically different from the corresponding condition in the presence of FBS, $p < 0.05$.

period, l-GO sheets were again proven to be more cytotoxic than s-GO, with apoptosis being the predominant pathway of cell death (only a very small percentage of the cells were PI positive, *i.e.*, undergoing necrosis).

In addition to material agglomeration, two other potential artifacts in assessing cellular viability using fluorescent probes and a flow cytometry may stand out. The first one can be attributed to carbonaceous materials that could quench the fluorescence of the dyes[37] used to determine the mechanism of cell death. The second one is due to the intrinsic optical properties of the GOs (*i.e.*, intrinsic fluorescence used above), with false positive signals that could arise due to the presence of the material attached to the cellular surface or internalized by the cells. We thus made sure that all analyzed events that were found positive for cell death displayed a typical fluorescence pattern; that is, annexin V-stained cells should have a "green halo" due to the interaction of an annexin V molecule with phosphatidylserine exchanged from the inner to the outer side of the plasma membrane as a sign of early apoptosis (Figure 4b). On the other hand, PI staining appeared as an intracellular fluorescent signal as a result of its intercalation with DNA. Overall, the results suggested that treatment with l-GO was inducing consistently more adverse cell responses compared to s-GO. The difference between the two material types was even more pronounced when FBS was not present during the initial 4 h of exposure, causing cellular detachment even at concentrations as low as 1 μg/mL for l-GO w/o FBS (Figure S6).

Taken together, these results suggested that exposure to l-GO (w/FBS or w/o FBS) can lead to cell death as a result of cytotoxic responses, which were more pronounced under treatment in the absence of FBS. In contrast to s-GO treatment, the presence of FBS did not fully alleviate the cytotoxicity of l-GO. On the contrary, treating cells with s-GO induced cytotoxicity only in the absence of FBS, but not when FBS was present from the beginning of the treatment. In order to understand whether the observed effects of GOs were related to BEAS-2B cell type, we measured cytotoxic response induced in two more cell lines (murine macrophage cell line J774.1 and human breast cancer cell line MCF-7, Figure S11). In both cell types, a similar trend was observed with l-GO inducing a decrease in the number of viable cells in a more significant manner than s-GO, and treatment in the presence of FBS attenuating the observed cytotoxicity. Altogether, these results highlighted that protein coating can lead to protection against the reactive parts of graphene oxide, which is in agreement with previously published studies.[16,17,28,38] These data also demonstrated that some physicochemical features, such as lateral dimension, may be more dominant than others in determining the overall toxicological profile of nanomaterials.

s-GO- and l-GO-Induced ROS Production in BEAS-2B Cells. Various studies addressing the toxicological profile of engineered nanomaterials, including carbon-based materials, have reported that induction of oxidative stress is one of the main mechanisms leading to adverse effects induced by nanomaterials.[8,9,39−44] To determine whether the cytotoxic

activity observed with l-GO and s-GO could be correlated with an increased level of intracellular production of ROS, we performed two complementary assays: determination of the intracellular oxidation of a 2′,7′-dichlorofluorescein diacetate (DCF-DA) probe using spectrophotometry in a microplate reader and confocal microscopy, and intracellular oxidation of a hydroethidine (HE) probe using flow cytometry. As intracellular ROS production is an early event occurring after cell treatment with nanomaterials,[8] we exposed cells to either s-GO or l-GO for only 4 h, in the presence or absence of FBS before incubating cells with the appropriate dyes to perform the assays.

DCF-DA is a cell-permeable, nonfluorescent probe that becomes highly green-fluorescent upon oxidation with H_2O_2 or other oxidants inside the cell.[45] BEAS-2B cells exposed to both GOs were observed under a confocal microscope in order to accurately differentiate the signal from the oxidized probe from eventual interference of the material (Figure 5a and Figure S12). Bright green fluorescence distributed throughout the cell cytoplasm was clearly observed for the cells treated with s-GO w/o FBS and for the cells treated with l-GO (w/FBS or w/o FBS) (Figure 5a). Treatment with H_2O_2 for 2 h was used as a positive control for induction of intracellular oxidative stress. Fluorescence intensity was quantitatively measured using a microplate reader, showing a dose-dependent increase for all conditions (Figure 5b). In detail, cells treated with s-GO produced significantly more ROS when initially exposed to s-GO w/o FBS than s-GO w/FBS. For the treatment with l-GO, the presence of serum during the contact period only slightly reduced the increase in intracellular ROS production. Comparing s-GO and l-GO treatments, l-GO induced a higher production of intracellular ROS than s-GO when cells were exposed in the presence of FBS. In contrast, in the absence of FBS, the difference between s-GO and l-GO was less significant, with both GO samples inducing an increase in intracellular ROS production.

In order to confirm the DCF-DA results, intracellular oxidation of the HE probe was measured using flow cytometry. It has already been shown that flow cytometry might be more sensitive than a microplate reader for detecting fluorescence intensity associated with a population of cells.[46] In agreement with the DCF-DA results, a dose-dependent increase in cellular ROS production was observed for both s-GO (w/FBS or w/o FBS) and l-GO (w/FBS or w/o FBS) (Figure 5c). Treatment with s-GO was mainly causing elevated ROS levels when the cells were exposed in the absence of FBS. In contrast, l-GO induced a dose-dependent increase of cellular ROS production for concentrations as low as 5 μg/mL under both conditions (w/FBS or w/o FBS).

Pro-inflammatory Response Induced by l-GO and s-GO. The increase of intracellular levels of ROS could lead to two concomitant outcomes: cellular inflammation or activation of antioxidant defense by induction of the Nrf2 signaling pathway and production of phase II metabolizing enzymes.[8] Increased expression of genes coding for cytokines (such as IL-6, IL-8, IL-1α, and IL-1β) could be indicative of acute inflammatory response by nanomaterial-treated cells.[5,12,47,48] We therefore compared the expression of these four genes in untreated cells with their expression in cells treated with either l-GO or s-GO, using RT-qPCR (Figure 6). Low subtoxic concentrations of GOs were chosen (<10 μg/mL), and the inflammatory responses were measured 24 h after treatment. For all analyzed genes, high expression levels suggesting a pro-inflammatory response were observed only after treatment with

l-GO and in the absence of FBS. No changes in gene expression were observed for any other condition. To confirm these results, ELISA-based measurement of IL-6 and IL-8 secretion was performed (Figure S14). While more cytokine release was found with l-GO when compared to the s-GO, in agreement with our RT-qPCR data, the results obtained for IL-8 cytokine secretion for the highest concentration tested (i.e., 10 μg/mL) suggested an absence of dose−response relationship. This could be explained either by the absorption of cytokines by the GO materials (i.e., GO sheets acting as nanotraps, as reported previously with other nanomaterials[49,50] and as suggested by our evaluation of cytokine adsorption, data not shown) or by a post-transcriptional regulatory process.[51] In both cases, it would lead to a decrease of the cytokines that could be detected by ELISA.

Size-dependent secretion of cytokines in response to GO exposure has been previously reported in macrophages,[12] with larger GOs inducing higher levels of IL-6, TNF α, and IL-1β via stimulation of NF-κB pathways in response to more robust interactions with cell membrane receptors than smaller GOs. In the present study, elevation of cytokines (Figure 6) was correlated with increased intracellular ROS (Figure 5) and consequent antioxidant response (Figure S13). ROS generation is involved in the phosphorylation of NF-κB pathways, which may upregulate the production of IL-1β, IL-6, and IL-8 in epithelial cells.[52−54] In a previous study, both large GO and small GO were found to induce equal levels of IL-1β in a THP-1 macrophage model (small GO slightly higher than large GO), but large GO was found to induce twice the amount of TGF-β1 induced by small GO in a BEAS-2B cell model.[5] These in vitro results were correlated with in vivo data in mice showing higher levels of IL-1β in broncho-alveolar lavage fluid (BALF) in animals treated with small GO (at least the first 3 days), while TGF-β1 levels in BALF and deposition of collagen in lungs were higher in mice treated with large GO than in small GO-treated animals. All effects were related to lysosomal damage, mediating the activation of inflammasomes.

IL-1α is constitutively expressed in the pulmonary epithelium, enabling the initiation of the inflammatory process before IL-1β is activated.[55] When epithelial cells lose their membrane integrity (as suggested by LDH assay results, Figure 3b, where l-GO w/o FBS treatment elicited higher membrane damage), IL-1α is released as a danger-associated molecular pattern (DAMP) or alarmin, which may bind to various receptors in neighboring cells, including toll-like receptors (TLRs) and IL-1R1.[55] Therefore, the dose-dependent increase of IL-1α and IL-1β found only in cells treated with l-GO w/o FBS (already at 10 μg/mL) and not in cells treated with l-GO w/FBS suggests that FBS coating of the GO sheets inhibits the inflammatory response by acting on a membrane-mediated pathway.

Plasma Membrane Interactions and Uptake of GO by BEAS-2B Cells. Altogether, these results show that the presence of FBS was not sufficient to mitigate the dose-dependent cytotoxicity, ROS generation, and inflammation induced by l-GO, while it was the case for s-GO. In order to understand the mechanism of GO-induced cellular responses, we first assessed whether ROS generation was an intrinsic property of the GOs. Using high-resolution electron paramagnetic resonance (EPR) to measure the amount of free radicals (i.e., unpaired electrons) present in the GO samples dispersed in the cell culture medium in the presence or absence of FBS, a single resonance peak was identified (Figure S15),

confirming the highest presence of carbon radicals in l-GO sheets dispersed in the cell culture medium in the absence of FBS. These radicals are known to originate from the hydrolysis of epoxy groups present on the surface of the sheets and are stabilized by the π-conjugated network on the basal plane of the GO.[56,57] A lower amount of carbon radicals was detected for the s-GO dispersed in the same conditions (Figure S15), while the presence of FBS in the cell culture medium attenuated significantly the intrinsic capacity of the GO to generate carbon radicals, most likely due to the surface coating of the sheets and decreasing surface reactivity of the materials. Lipid peroxidation is a potential outcome of the interaction between reactive carbon radicals of GO with cell membrane lipids.[57] Therefore, we assessed lipid peroxidation induced by GO using a fluorescent probe (Bodipy 591/581 C11) that was visualized by confocal live imaging. We observed a limited lipid peroxidation as early as 2 h after exposure of the cells to s-GO and l-GO, but only when materials were dispersed in the absence of FBS (Figure S16). When GO sheets were dispersed in the presence of FBS, no lipid peroxidation was observed. This finding is in agreement with the hypothesis that interaction of GO with biomolecules from the serum decreases the surface reactivity of the sheets, which in turn can result in the difference in adverse effects (especially levels of detected ROS) between coated and uncoated GOs.

In order to explain the differences between toxic responses of large *versus* small GO, we investigated GO sheet interaction with the cell membrane and their uptake. Even though both GO types were efficiently taken up (Figure S17), interactions with the plasma membrane were significantly different among different GO types and treatment conditions. Small GO sheets dispersed in the presence of FBS were predominantly found to localize in perinuclear vesicular structures in the cytoplasm. In all other treatment conditions, we observed ruffling and highly dynamic interactions of the membrane with the sheets, leading to the formation of invaginations and intracellular vesicles filled with materials. Membrane interactions and the presence of vesicles were more pronounced after treatment with l-GO compared to s-GO, especially in the absence of FBS. Efficient uptake of GO sheets (either l-GO or s-GO) did not induce lysosomal disruption, indicating that toxicity was not mediated *via* the lysosomal pathway (Figure S18). Taking into account these observations, we hypothesized that a greater toxic effect of micrometre-sized l-GO sheets might arise from their specific interaction with the plasma membrane and impact on the actin cytoskeleton. We used high-resolution live confocal imaging to observe interactions of the label-free sheets with the plasma membrane (Figure 7) and their impact on the underlining actin cytoskeleton (Figures S19 and S20). Treatment with s-GO in the presence of FBS did not elicit morphological changes to the plasma membrane of the cells. However, for all other treatment conditions, particularly for the l-GO sheets in the absence of FBS, a greater perturbation of the plasma membrane was observed, as indicated in Figure 7. These observations correlated with a reorganization of actin filaments, constituting spherical bundles enriched in actin that were more visible around GO agglomerates (Figures S19 and S20, middle section of the cell). Our results are in agreement with previous reports showing that GBMs are able to induce cytoskeleton remodeling, ultimately affecting cell motility, viability, and signaling pathways.[58,59] Together with the greater membrane interactions depicted in Figure 7, we can conclude that l-GO induced more actin cytoskeleton remodeling in the region of
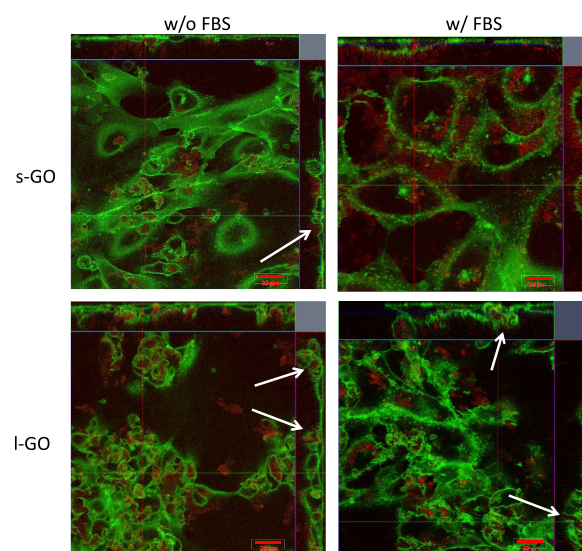

Figure 7. Interactions of s-GO and l-GO with the plasma membrane of BEAS-2B cells. Cells were treated with 50 μg/mL of the material in the presence or absence of 10% FBS during the first 4 h, for a total period of 24 h. After staining of the plasma membrane, interactions with the material were assessed using a high-resolution confocal live imaging microscope. Staining of the cells is as follows: Green = cell membrane, red = materials, either s-GO or l-GO. White arrows indicate regions of the plasma membrane interacting with the GO (ruffling and invaginations of the membrane). Scale bar = 10 or 20 μm.

the cell membrane that was interacting with the sheets than s-GO (Figure S20). Under these conditions, actin remodeling resulted in higher membrane blebbing and increased apoptotic cell death, as shown in Figure 4.[60] Hence, physical interaction in relation to dimensions (*i.e.*, larger materials interacting more with the cell membrane) might be a major determinant for the biological impact of GO sheets.

L-GO-Induced Granulomatous Response in the Lungs in Vivo. To validate the *in vitro* results, the pro-inflammatory effect of l-GO and s-GO was further studied *in vivo* by administering GO sheets, dispersed in an aqueous solution of 5% dextrose, to C57BL/6 mice *via* intranasal instillation. A dose of 50 μg per mouse was selected, in agreement with previous reports demonstrating the lung pathogenicity of carbon nanotubes or graphene nanoplatelets.[61,62] On the basis of our previous studies using other administration routes (intravenous or intraperitoneal injections), where s-GO had minimal toxicity, we hypothesized that l-GO would induce a stronger inflammatory response in the lungs.[63,64]

Lung histopathology at days 1, 7, and 28 after exposure indicated a significant reaction by the lung parenchyma to both GO materials (Figure 8a), characterized by alveolar wall thickening and formation of granulomas. These features are indicative of infiltration of immune cells, whose agglomeration to the site where the materials are deposited describes a common foreign body reaction.[65] In agreement with our *in vitro* experiments, l-GO induced more foreign body reaction than s-GO (Figure 8a and b). At days 1, 7, and 28, l-GO induced more cell infiltration than s-GO, leading to larger granulomas by day 28 (Figure 8a). The greater impact of l-GO could be explained by the larger size of l-GO agglomerates in the lung sections, as evidenced by optical microscopy and confirmed by Raman spectroscopy imaging (Figures 8c and S21). A key mechanism
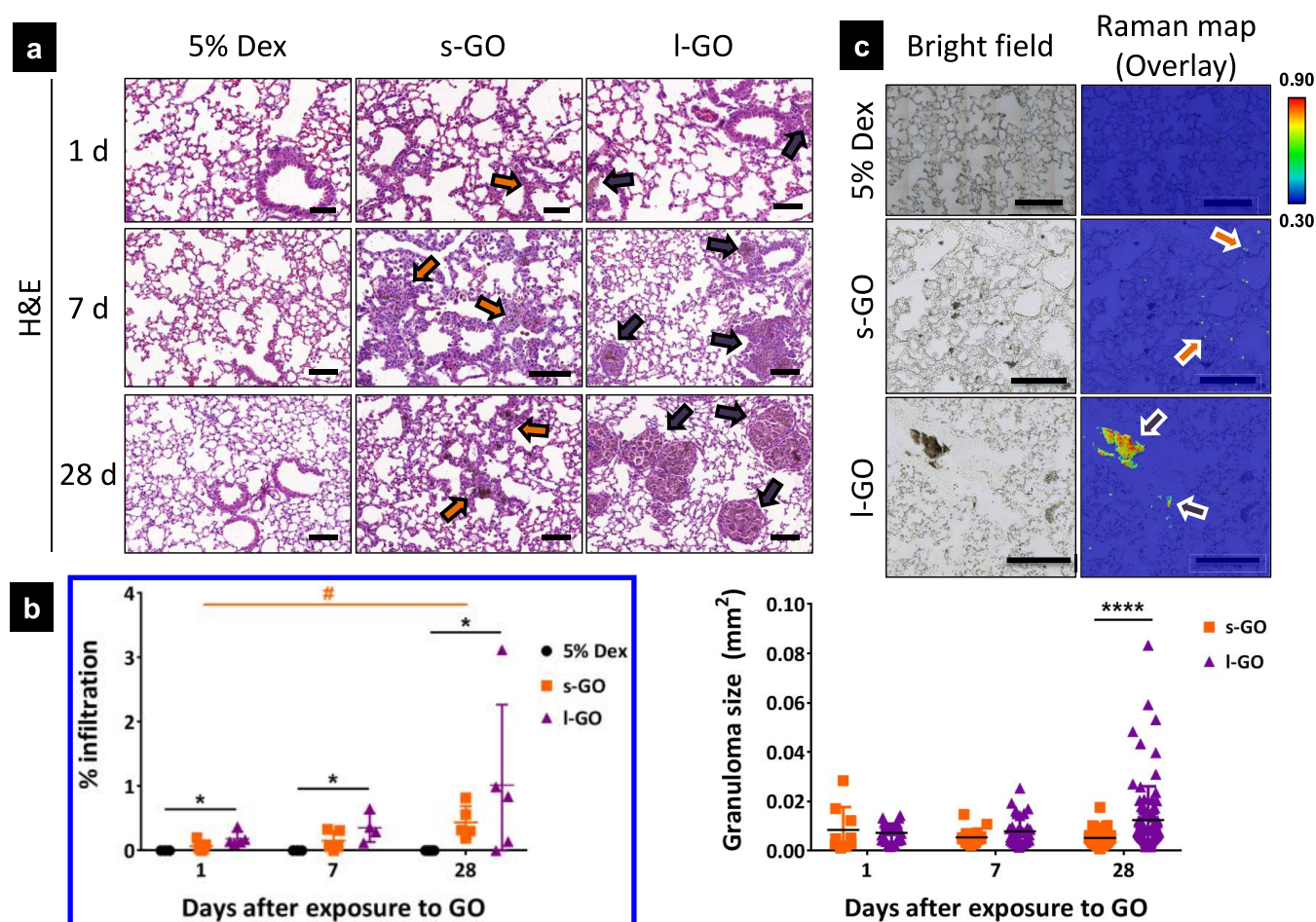
Figure 8. Granulomatous response in the lungs over a period of 28 days after intranasal instillation of s-GO and l-GO. C57BL/6 mice were instilled with 50 μg of s-GO or l-GO, and their lungs were extracted at 1, 7, and 28 days after administration. (a) Lung sections were obtained for histopathological analysis using H&E staining. Arrows indicate alveolar thickening and formation of granulomas due to the presence of the material. (b) Areas of alveolar thickening and formation of granulomas due to the presence of GO were manually segmented using ImageJ image analysis software. Total area of these histological features was measured and normalized to the total area of the lung section (% infiltration). Cell infiltration results are represented as the percentages obtained for each animal, followed by average ± SD. Size of each segmented area was also plotted (granuloma size), followed by average ± SD. Data were analyzed at each time point using a Kruskal–Wallis test with *post hoc* Dunn's multiple comparisons test. Difference between treatments at specified time points with $p < 0.05$ were considered statistically significant: *$p < 0.05$, ****$p < 0.0001$.

of the foreign body reaction consists in the fusion of multiple macrophages to form giant cells, which are then able to internalize particles larger than 10 μm.[65] While l-GO-induced granulomas seemed to increase in size from day 7 to 28, s-GO-induced granulomas did not. This difference is likely to result from the smaller size of s-GO agglomerates, which are more easily phagocytosed by individual macrophages, as suggested by Raman spectroscopy imaging, which showed s-GO signal within circular features, suggesting cell uptake. These *in vivo* findings were in agreement with RT-qPCR analysis of GO-treated BEAS-2B cells (Figures 6, S13, and S14), in which pro-inflammatory cytokines and growth factors such as GM-CSF were upregulated.

The results reported in the present study highlight the role of GO lateral dimensions, acting as a major factor determining cytotoxicity or other adverse biological responses, including plasma membrane interactions, actin filament remodeling, oxidative stress, and inflammation. In agreement with the literature, protein coating of the tested nanomaterials was confirmed to have a positive outcome for the treated cells, with either a decrease (in the case of l-GO) or a complete suppression (in the case of s-GO) of the adverse effects such as lipid peroxidation of the plasma membrane or increased intracellular ROS levels. This is in agreement with previous studies showing the beneficial effects of serum proteins in carbon nanomaterial toxicity.[17,66] Protein coating of GOs is thought to cause electrostatic repulsion between the sheets and therefore prevent their agglomeration and aggregation.[67] By improving the dispersibility of GO, serum proteins make GO sheets less prone to interact with the cell membranes and less toxic.[17,67]

However, even in the presence of serum, large micrometer-sized materials were still causing more harm to the cells than small nanometer-sized ones, which were harmless under these conditions. This was obvious from the live imaging of the cells exposed to the materials, showing that the adverse effects of l-GO sheets occur as a result of their interaction with the plasma membrane, which induced remodeling of the actin cytoskeleton, even in the presence of FBS from the beginning of the treatment. The absence of FBS during the first 4 h of treatment amplifies the effects observed in the presence of FBS, as a result of a higher surface reactivity of the uncoated GO sheets when

compared to coated materials. This increased reactivity leads to higher oxidative stress, lipid peroxidation, and cell death as mentioned above. The link between lateral dimensions of GO and both inflammation and oxidative stress has been established before using various cell types.[5,12,48] In the majority of these studies, large materials (>1 μm) induced more adverse effects than smaller materials (<500 nm). While the pronounced deleterious impact of large GO sheets has been linked to their interaction with TLRs of macrophages,[12,48] small GO sheets were associated with weaker inflammatory response due to their lower adsorption to the plasma membrane.[48] In this work, we found a higher upregulation of IL-1α, IL-1β, IL-6, and IL-8 with large GOs in comparison to small GOs. This inflammatory response was associated with both oxidative stress and destabilization of the plasma membrane, which was shown to induce reorganization of the cytoskeleton, in particular in treatments with l-GO w/o FBS, in agreement with previous reports.[60,68,69]

A decade of nanotoxicology research has evidenced ROS production and activation of pro-inflammatory signaling pathways as two major molecular mechanisms associated with the adverse effects and cytotoxicity of engineered nanomaterials. In various studies, the oxidative stress paradigm was shown to be a valid indicator to allow comparison between the cytotoxic responses induced by ambient or engineered nanoparticles and nanomaterials.[8−10] In this regard, graphene-based materials including the GOs tested here are not different from any other nanomaterial, and their biological impact can be explained and predicted using this paradigm.[48,70] Considering that the two types of GOs used here differed only in their lateral dimensions, the present study demonstrated the critical importance of this parameter compared to serum protein coating.

CONCLUSIONS

In the present study the intrinsic fluorescence of GO was exploited to visualize behavior of the cells in response to the material in real time using live-cell confocal imaging. Furthermore, protein coating of GO was shown to have a secondary role in comparison to the effect of lateral dimensions in inducing oxidative-stress-mediated cellular responses. Although both GO types were internalized efficiently by the cells, large micrometer-sized material was found to be more damaging than small nanometer-sized material, leading to greater plasma membrane interactions correlated with elevated ROS levels, pro-inflammatory response, and higher cytotoxicity. Coating with proteins from FBS alleviated lipid peroxidation of the plasma membrane and decreased intracellular ROS levels. However, protein coating was not enough to entirely mitigate the toxicity and inflammatory response induced by l-GO. *In vitro* results were validated *in vivo*, as l-GO was more prone to induce a pulmonary granulomatous response in mice compared to s-GO. Therefore, we concluded that lateral dimensions of GO played a more important role than serum protein coating in governing biological responses to the material.

METHODS AND EXPERIMENTAL

Production and Characterization of the l-GO and s-GO. *Production.* Materials were prepared following a procedure described previously[20] based on a modified Hummers method and allowing the production of endotoxin-free materials.[22] The starting graphite used in the reaction was graphite powder (product code #282863, <20 μm, synthetic, Sigma-Aldrich, Merck Sigma, UK). Following this chemical

exfoliation procedure, materials corresponding to the "large" GO sample (l-GO) were produced with final concentrations ranging between 1 and 2 mg/mL, achieving a yield of *ca.* 15−20%.[22] Large GO materials were then sonicated in a bath sonicator (VWR, 80 W) for 5 min and centrifuged at 13 000 rpm for 5 min at room temperature to prepare the "small" GO sample (s-GO).

Optical Microscopy. Bright-field microscopy using a PrimoVert inverted optical microscope (Carl Zeiss, UK) using an objective with 200× magnification was performed to determine the lateral dimension distribution of the l-GO (sheets in the microsized range) and to verify the size reduction of the s-GO (below Abbe's diffraction limit). Hundreds of particles were manually measured by determining the Feret diameter using ImageJ (NIH, USA).

Transmission Electron Microscopy. TEM was performed using a FEI Tecnai 12 BioTwin microscope (FEI, The Netherlands) at an acceleration voltage of 100 kV. Images were taken with a Gatan Orius SC1000 CCD camera (GATAN, UK). A 20 μL sample (100 μg/mL) was placed on a Formvar/carbon-coated copper grid (CF400-Cu) (Electron Microscopy Services, UK). Filter paper was used to remove excess liquid.

Atomic Force Microscopy. AFM images were acquired using a Multimode 8 AFM (Bruker, UK) in tapping mode in air with a J-type scanner, Nanoscope V8 controller, and an OTESPA silicon probe (Bruker, UK). Samples were prepared by depositing 20 μL of a 100 μg/mL GO suspension on a freshly cleaved mica surface (Agar Scientific, Essex, UK) coated with poly-L-lysine 0.01% (Sigma-Aldrich, Merck Sigma, UK) and allowed to adsorb for 2 min. Excess unbound materials were removed by gently washing with Milli-Q water and then allowed to dry in air. Lateral dimension and thickness distributions of GO sheets were carried out using Nanoscope Analysis software (version 1.40, Bruker, UK).

UV/Visible Spectroscopy. UV−vis absorbance spectra were obtained for GO samples at 7.5 to 20 μg/mL using a Varian Cary 50 Bio UV−vis spectrophotometer (Varian Inc., Agilent Technologies, UK). Dual beam mode and baseline correction were used throughout the measurements to scan the peak wavelength and maximum absorbance between 200 and 800 nm.

Raman Spectroscopy. Samples were prepared for analysis by drop casting ~20 μL of GO (100 μg/mL) dispersion onto a glass slide. Samples were left to dry for at least 2 h at 37 °C. Spectra were collected using a DXR micro-Raman spectrometer (Thermo Scientific, UK) using a 50× objective lens and using a λ = 633 nm laser with an exposure time of 25 s at an intensity of 0.4 mW. Spectra were averaged over five independent locations and considered between 250 and 3500 cm^{-1}, enabling visualization of the D and G scatter bands. The average I_D/I_G ratio for each sample was then calculated.

Zeta-Potential Measurements. Electrophoretic mobility (μ) was measured using a ZetaSizer Nano ZS (Malvern Instruments, UK) after dilution of samples with water (100 μg/mL) in disposable cuvettes (Malvern Instruments, UK). Default instrument settings and automatic analysis were used for all measurements, performed at room temperature with a backscattering angle of 173°. The equipment software converted automatically the μ to zeta-potential (ζ) values by Henry's equation. All values for samples prepared are triplicate measurements, and values were mean ± SD.

Thermogravimetric Analysis. The weight loss of GO samples was performed by TGA using a Pyris 6 (PerkinElmer Ltd., UK). Lyophylized GO (1−2 mg) was weighed into a ceramic crucible and analyzed from 25 to 995 °C at 10 °C/min, under a nitrogen flow of 20 mL/min.

X-ray Photoelectron Spectroscopy. The composition of GO surfaces was studied by XPS at the NEXUS facility (the UK's National EPSRC XPS Users' Service, hosted by nanoLAB in Newcastle-upon-Tyne). XPS was recorded using a Thermo Theta Probe XPS spectrometer with a monochromatic Al Kα source of 1486.68 eV. The survey XPS spectra were acquired with a pass energy (PE) of 200 eV, 1 eV step size, and 50 ms dwell time and averaged over five scans. The etching was 90 s. High-resolution C 1s XPS spectra were acquired with a PE of 40 eV, 0.1 eV step size, and 100 ms dwell time and averaged over 20 scans. Spectra from insulating samples have been

charge-corrected by shifting all peaks to the adventitious carbon C 1s spectral component binding energy set to 284.6 eV. CasaXPS software (Casa Software Ltd., UK) was used to process the spectra acquired at NEXUS. For the deconvolution of the different components, the CasaXPS software was used and the different regions were assigned according to NIST's XPS and laSurface databases, after subtracting the background using a Shirley algorithm:

$\pi-\pi^*$: 292.0−290.0 eV

O−C≡O: 290.0−288.6 eV

C≡O: 287.8−286.8 eV

C−O: 286.6−285.5 eV

C−C and C≡C: 284.6−284.5 eV

All peaks were deconvoluted using a Gaussian:Lorentzian (70:30) function, apart from the peak for C−C and C≡C, which was fitted by an asymmetric Lorentzian function. Each deconvoluted peak, except that of the $\pi-\pi^*$ contribution, was constrained to the same full width at half-maximum value.

Endotoxin Content of the Samples. Materials were tested for their endotoxin content based on the method described previously.[21] In brief, cells were exposed to l-GO and s-GO for 24 h in order to allow the production of TNF-α in the presence or absence of polymyxin B. When added into the interaction of GO with cells, polymyxin B would prevent the production of TNF-α if this production is mediated by endotoxin and not the result of sterile inflammation due to the GO sheets.

Electron Spin Resonance Spectroscopy. Continuous-wave EPR measurements were carried out at room temperature, using an EMX-Micro X-band spectrometer (Bruker, UK) operating at a frequency of ~9.86 GHz, center field at 3520 G, and attenuator at 30 dB. Approximately 1.3 mg of lyophilized powder of each GO material dispersed in the cell culture medium in the presence or absence of FBS (50 μg/mL) and then freeze-dried was placed in the bottom of an EPR quartz tube. The field was calibrated using 2,2-diphenyl-1-picrylhydrazyl (DPPH) as a standard sample with $g = 2.0036$. The carbon radical concentration was estimated by calculating the area of the high-resolution EPR spectra by double integration and calculating the number of spins relative to the DPPH standard. Obtained spin concentrations were normalized by the respective masses of GO samples and standard, yielding radical concentrations in mmol/g.

Agglomeration of GO in Cell Culture Medium. GO samples were incubated (100 μg/mL) for 24 h at room temperature in RPMI 1640 cell culture medium (Sigma-Aldrich, Merck Sigma, UK) supplemented with 20 mM glutamine (Sigma-Aldrich, Merck Sigma, UK), 10% FBS (Gibco, Thermo Fisher Scientific, UK), 1000 units penicillin, and 1 mg/mL streptomycin (Sigma-Aldrich, Merck Sigma, UK). GO agglomerates were then obtained by centrifugation at room temperature, for 30 min at 13 000 rpm. The supernatants containing the cell culture medium were discarded, and the GO pellets were gently resuspended in Milli-Q water. This washing step was repeated once in order to remove excess unattached biomolecules and electrolytes, enabling the characterization of GO agglomerates by AFM, dynamic light scattering, and zeta potential measurements, as described above.

Cell Culture. Human epithelial bronchial immortalized cells (BEAS-2B, CRL-9609, ATCC, LGC standards, UK) were maintained in RPMI 1640 cell culture medium (Sigma-Aldrich, Merck Sigma, UK) supplemented with 20 mM glutamine (Sigma-Aldrich, Merck Sigma, UK), 10% FBS (Gibco, Thermo Fisher Scientific, UK), 1000 units penicillin, and 1 mg/mL streptomycin (Sigma-Aldrich, Merck Sigma, UK) at 37 °C in a humidified 5% CO$_2$ incubator. Cells were passaged twice a week using a 0.05% Trypsin−EDTA solution (Sigma-Aldrich, Merck Sigma, UK) when reaching 80% confluence. Activity of trypsin was stopped using 10% FBS. All experiments were done using cells with a passage number between 25 and 35.

Cell Culture Treatment. Depending on the experiment, cells were seeded in 96- (modified LDH and DCF-DA assay), 12- (cell count, modified LDH assay, HE oxidation), or six- (PI/annexin V staining,

PCR experiments) well plates (Corning, Costar, Sigma-Aldrich, Merck Sigma, UK) and treated with GO when reaching 60−80% confluence. Cell treatments were performed after dispersing the GO in RPMI 1640 cell culture medium in either the absence of FBS (w/o FBS) or the presence of 10% FBS (w/FBS). Material suspensions were thoroughly vortexed shortly before the treatment. For cells treated with GO dispersed in FBS-free medium, the cell culture medium was supplemented with 10% FBS 4 h after treatment. Incubations with GOs were maintained for 2, 4, 24, or 72 h. All experiments were repeated at least twice.

Cell Count Experiment. For cell counting, cells were seeded and treated in triplicates in 12-well plates. After 24 h of treatment using the indicated concentrations of GOs (w/FBS or w/o FBS), supernatants were removed and cells were collected using 0.05% Trypsin−EDTA. After 5 min of incubation, the action of Trypsin−EDTA was blocked using 10% FBS. Cells harvested from each well were transferred to a separate 1.5 mL microtube, and 10 μL of Trypan Blue (0.4% solution, Sigma-Aldrich, Merck Sigma, UK) was mixed with 10 μL of cells. Live cells (unstained for Trypan Blue) were counted using a Neubauer counting chamber. For each condition, cells were treated in triplicates and cell count was repeated twice.

PI/Annexin V-Alexa Fluor488 Conjugate Assay. For the PI/annexin V staining experiment, cells were seeded and treated in six-well plates after reaching 60−80% confluence. After 24 h of treatment, supernatants were removed and cells were gently washed once with phosphate-buffered saline (PBS) containing Ca^{2+}/Mg^{2+} (Sigma-Aldrich, Merck Sigma, UK). Annexin V staining was performed according to the instructions of the manufacturer (Molecular Probes, Thermo Fisher Scientific, UK). In brief, cells were trypsinized for 5 min, centrifuged at 1500 rpm for 5 min, then resuspended in 50 μL of annexin binding buffer (Molecular Probes, Thermo Fisher Scientific, UK), and stained with 1 μL of annexin V−Alexa Fluor488 conjugate for 20 min at 25 °C. Propidium iodide (1 mg/mL, Sigma-Aldrich, Merck Sigma, UK) was added shortly before the analysis to the final concentration of 1.5 μg/mL. At least 2500 cells were analyzed using the Amnis ImageStream platform (Amnis ImageStream MKII, Merck, UK) and Inspire system software (Amnis, Merck, UK). Camera magnification was 60×; the 488 nm excitation laser was set to 60 mW; the 785 nm excitation laser was set to 0.02 mW. Images were acquired with a normal depth of field, providing a cross-sectional image of the cell with a 2.5 μm depth of focus. The results were analyzed by IDEAS software (Amnis).

Confocal Microscopy. *Plasma Membrane Staining.* Cells were seeded in a Cellview cell culture dish (627870, Greiner Bio-One Ltd., UK) and treated when reaching 60−80% confluence with 50 μg/mL s-GO (w/FBS or w/o FBS) or l-GO (w/FBS or w/o FBS). For w/o FBS conditions, 10% FBS was added to each well after 4 h. CellMask green plasma membrane stain (C37608, Thermo Scientific, UK) was added to the cell culture medium containing GO sheets before treatment (dilution 1:2500) and added to the cells at the same time as the GO. After 2 h of treatment, time lapses were set to start the live-cell imaging. Five positions were chosen for each condition, and the experiment was repeated three times. Cells were examined under a Zeiss 780 multiphoton confocal laser scanning microscope using a 40× objective with a time lapse mode. Excitation wavelengths for the CellMask green plasma membrane stain and GOs were 488 and 594 nm, respectively. Emission maximum for the CellMask green plasma membrane stain was 520 nm, while emission wavelength for the GOs was 620−690 nm. Time lapse videos and images were processed using Zeiss microscope software ZEN.

DCF-DA Staining. Cells were seeded in a Cellview cell culture dish (627870, Greiner Bio-One Ltd., UK), washed once with PBS (with Ca^{2+}/Mg^{2+}, Sigma-Aldrich, Merck Sigma, UK), and preloaded with 20 μM DCF-DA dye for 45 min at 37 °C, in a humidified 5% CO$_2$ incubator. After preloading, cells were washed in PBS (with Ca^{2+}/Mg^{2+}, Sigma-Aldrich, Merck Sigma, UK) and treated with 50 μg/mL of s-GO and l-GO in the presence or absence of FBS for 4 h or with 1 mM H$_2$O$_2$ for 2 h (as a positive control). After 4 h of treatment, cells were washed in PBS (with Ca^{2+}/Mg^{2+}, Sigma-Aldrich, Merck Sigma, UK) and imaged using a Zeiss 780 confocal laser scanning microscope

using a 40× objective. Excitation wavelengths for the DCF-DA dye and GOs were 488 and 594 nm, respectively. Emission maximum for the DCF-DA dye was 520 nm, while emission wavelength for the GOs was 620−690 nm. Images were processed using Zeiss microscope software ZEN.

Lysotracker Blue Staining. Cells were seeded in a Cellview cell culture dish (627870, Greiner Bio-One Ltd., UK) and treated when reaching 60−80% confluence with 100 μg/mL s-GO (w/FBS or w/o FBS) or l-GO (w/FBS or w/o FBS) for 24 h. After treatment, cells were stained with 75 nM LysoTracker Blue DND-22 (L7525; Thermo Fisher Scientific, UK) for 30 min, in a humidified 5% CO_2 incubator. Imaging of the cells was performed using a Zeiss 780 confocal laser scanning microscope and a 40× objective. Excitation/emission wavelengths of 373/422 nm (DAPI filter set) were used. Images were processed using Zeiss microscope software ZEN.

Lipid Peroxidation Assessed by Bodipy 581/591 C11 Staining. Cells were seeded in a Cellview cell culture dish (627870, Greiner Bio-One Ltd., UK) and treated when reaching 60−80% confluence with 50 μg/mL of s-GO or l-GO in the presence or absence of FBS for 2 h. Cumene hydroperoxide treatment (100 μM, for 2 h) was used as a positive control for lipid peroxidation. After treatment, cells were stained using 10 μM Bodipy 581/591 C11 (C10445, Image-iT lipid peroxidation kit, Thermo Fisher Scientific, UK) for 20 min at 37 °C, in a humidified 5% CO_2 incubator. Imaging of the cells was performed using a Zeiss 780 confocal laser scanning microscope and a 40× objective. Excitation/emission wavelengths of 581/591 nm (Texas Red filter set) and 488/510 nm (traditional FITC filter) were used to detect oxidized (green) and nonoxidized (magenta) signal from the probe. The ratio of the emission fluorescence intensities at 590 to 510 nm gives a read-out for cellular lipid peroxidation. Images were processed using Zeiss microscope software ZEN.

Actin Filament Staining. Cells were seeded in Cellview cell culture dish (627870, Greiner Bio-One Ltd., UK) and treated when reaching 60−80% confluence with 50 μg/mL of s-GO or l-GO in the presence or absence of FBS for the first 4 h of treatment. After treatment, cells were fixed using 3.7% PFA for 10 min at room temperature, permeabilized using 0.1% Triton X-100 in PBS for 5 min, and stained with 4.5 nM Alexa Fluor 488 Phalloidin dye (A12379, Thermo Fisher Scientific, UK). After staining cells were washed three times in PBS and observed using a Zeiss 780 confocal laser scanning microscope and a 40× objective. Excitation wavelengths for the Alexa Fluor 488 Phalloidin dye and GOs were 488 and 594 nm, respectively. Emission maximum for the Alexa Fluor 488 Phalloidin dye was 520 nm, while emission wavelength for the GOs was 620−690 nm. Time lapse videos and images were processed using Zeiss microscope software ZEN.

Modified LDH Assay. For the LDH assay, cells were seeded and treated for 24 h in triplicates or sextuplicates in 12- or 96-well plates, respectively. The LDH assay was modified to avoid any interference coming from the interaction between GO and the assay reagents.[33] Briefly, LDH content was assessed in intact cells that survived the treatment, instead of detecting the amount of LDH released in the media upon treatment. Media was aspirated and cells were lysed with 100 μL of lysis buffer for 45 min at 37 °C to obtain cell lysates, which were then centrifuged at 4000 rpm for 20 min in order to pellet down GOs. A 50 μL amount of cell lysate supernatant was transferred to a new 96-well plate and mixed with 50 μL of LDH substrate mix (CytoTox 96 nonradioactive cytotoxicity assay, Promega, UK) and left to react for 7−15 min at room temperature, after which 50 μL of stop solution was added.

Cell Survival %

$$= (\alpha_{490nm} \text{ of treated cells}/\alpha_{490nm} \text{ of untreated cells}) \times 100$$

The absorbance was read at 490 nm using a spectrophotometer plate reader (FLUOstar Omega, BMG Labtech, UK). The amount of LDH detected represented the number of cells that survived the treatment. The percentage cell survival was calculated using the equation above.

DCF-DA Assay. For the DCF-DA assay, cells were seeded and treated in sextuplicates in 96-well plates for 4 h. After treatment, cells were gently washed with 100 μL per well of prewarmed PBS (with

Ca^{2+}/Mg^{2+}, Sigma-Aldrich, Merck Sigma, UK) in order to remove the materials and subsequently incubated with 20 μM DCF-DA (Sigma-Aldrich, Merck Sigma, UK) diluted in PBS (with Ca^{2+}/Mg^{2+}) for 45 min at 37 °C, in a humidified 5% CO_2 incubator. After incubation with the dye, fluorescence intensity was read using a spectrofluorimeter microplate reader (FLUOstar Omega, BMG Labtech, UK) with a 488 nm excitation laser and collecting emission at 520 nm.

HE Oxidation. For the HE oxidation experiment, cells were seeded and treated in triplicates in 12-well plates using the indicated concentrations of GO sheets for 4 h. After treatment, supernatants were aspirated and cells gently washed once with 1 mL per well of prewarmed PBS (with Ca^{2+}/Mg^{2+}, Sigma-Aldrich, Merck Sigma, UK). Cells were detached using 0.05% Trypsin−EDTA solution (Sigma-Aldrich, Merck Sigma, UK) for 5 min, then centrifuged for 5 min at 1500 rpm; supernatants were then aspirated, and pellets containing cells were resuspended in 1 μM hydroethidine (Sigma-Aldrich, Merck Sigma, UK) for 20 min. Ten thousand cells were analyzed on a BD FACSVerse flow cytometer using 488 nm excitation and 620 nm band-pass filters for HE detection. GOs alone were run in order to set up the gates including the cell population for the analysis and eliminate the signal coming from free materials or cell debris. Cells treated with the materials, but unstained with HE, were also run in order to ensure that the detected signal was not due to the inherent fluorescence of GOs. Percentages of unstained cells and cells stained with HE were calculated.

RT-qPCR Analysis. BEAS-2B cells were seeded in six-well plates and treated in triplicates with the indicated concentrations of either l-GO or s-GO for 24 h. After treatment, supernatants were removed and total RNA was extracted with an *ad hoc* kit (Aurum Total RNA mini kit, Bio-Rad, UK) according to the manufacturer's instructions. The concentration of total RNA was determined by measuring the optical density on a Biophotometer Plus spectrophotometer (Eppendorf AG, Germany); the purity was checked measuring both absorbance ratios 260 nm/280 and 260 nm/230 nm, with expected values between 1.8 and 2.0. First-strand cDNA was then prepared from 1 μg of RNA in a total volume of 20 μL using the iScript cDNA synthesis kit (Bio-Rad, UK). Real-time PCR was performed using the CFX96 real-time PCR detection system (BioRad, UK). The cDNA reactions contained 2 μL of Fast SYBR Green Master Mix (BioRad, UK), each primer at 200 nM, and 2 μL of cDNA from reverse transcription PCR in a 25 μL reaction. After an initial denaturation step at 95 °C for 10 min, amplification was carried out with 40 cycles of denaturation at 95 °C for 10 s and annealing and elongation at 60 °C for 30 s. Amplification was followed by a melting curve analysis to confirm PCR product specificity. No signals were detected in no-template controls. All samples were run in triplicate, and the mean value of each triplicate was used for further calculations. Relative gene expressions were calculated using the $\Delta\Delta CT$ method. The quantity of GAPDH (housekeeping) transcript in each sample was used to normalize the amount of each transcript, and then the normalized values were further normalized to the expression value in untreated cell samples to calculate a fold change value.

ELISA Assay. For the ELISA assay, cells were seeded in 96-well plates and treated in triplicates at 70% confluency, with the indicated concentrations of either s-GO or l-GO for 24 h. After the treatment, supernatants were collected and centrifuged at 10000g for 10 min at 4 °C to pellet down the GO. Supernatants were collected after centrifugation, and concentration of cytokines was determined using human IL-6 and IL-8 kits (BD Biosciences, UK) according to the manufacturer's recommendations.

***In Vivo* Experiments.** *Experimental Animals.* Six- to 8-week-old female C57BL/6 mice (Envigo, UK) were used in the present study, in accordance with the ARRIVE guidelines and after ethical approval from the UK Home Office, under Project License no. 70/7763. Animals were kept in IVC cages in groups of 5 with free access to food and water, on a normal 12 h light and dark cycle. All experiments were conducted using 3 animals per group, except at longer time points, where 5 animals were assigned to each group.

Intranasal Instillation. For the intranasal instillation of GO, mice were kept under light anesthesia (2.5% isoflurane with oxygen flow of

Table 2. Sequence of the Primers for the Genes Analyzed Using RT-qPCR

gene	accession no. (GenBank)	primer	sequence (5′ → 3′)
IL-6	NM_000600.4	forward	AGTGAGGAACAAGCCAGAGC
		reverse	GTCAGGGGTGGTTATTGCAT
CXCL8 (IL-8)	NM_000584.3	forward	CGGAAGGAACCATCTCACTG
		reverse	AGCACTCCTTGGCAAAACTG
TNF	NM_000594.3	forward	TGGGATCATTGCCCTGTGAG
		reverse	GGTGTCTGAAGGAGGGGGTA
IL1β	NM_000576.2	forward	AGCTGATGGCCCTAAACAGA
		reverse	CCTGAAGCCCTTGCTGTAGT
IL1α	NM_000575.4	forward	ACTGCCCAAGATGAAGACCA
		reverse	CCGTGAGTTTCCCAGAAGAA
HMOX1 (HO1)	NM_002133.2	forward	AGCTCTTTGAGGAGTTGCAGGA
		reverse	AGCTGAGTGTAAGGACCCATCG
CSF2 (GM-CSF)	NM_000758.3	forward	GCTGCTGAGATGAATGAAAC
		reverse	AGTCAAAGGGGATGACAAG
GAPDH	NM_002046.5	forward	CCACATGGCCTCCAAGGAGTAAGAC
		reverse	AGGAGGGGAGATTCAGTGTGGTGGG

2 L/min). Instillation of 50 μL was performed by pipetting approximately half of the volume in each nostril. Mice were held in a supine position, tilted to about 60°, in order to allow for the efficient entry of the whole volume. Mice were observed until full recovery, which occurred within 5 min after instillation. Both l-GO and s-GO materials were diluted to 1 mg/mL in an aqueous solution of 5% (m/v) dextrose in ultrapure water, totaling an instilled dose of 50 μg. The same volume of aqueous solution of 5% dextrose was administered as a vehicle control. The 5% dextrose solution was sterile filtered prior to dispersion of GO.

Dissection of Lungs. Mice were sacrificed at 1, 7, and 28 days after exposure to a single dose of GO by terminal anesthesia, using intraperitoneal injection of 0.2 mL of pentobarbitone. The thoracic cavity was then carefully excised and lungs were dissected. After gently rinsing in Hank's balanced salt solution (Gibco, Thermo Fisher Scientific, UK) to remove excess blood, the lungs were split in two different containers both undergoing an overnight fixation step in 4% (m/v) paraformaldehyde at 4 °C. The left lung used for histopathological analysis was then transferred to 70% (v/v) ethanol before paraffin embedding. The right lung used for Raman mapping was transferred to an aqueous solution of 30% (m/v) sucrose before snap-freezing in optical cutting temperature (OCT) compound.

Lung Histopathology. Paraffin-embedded lung sections with a thickness of 5 μm were obtained for hematoxylin and eosin (H&E) staining. Images were collected using a 20× objective under a Pannoramic 250 Flash slide scanner (3D Histech, Hungary), in bright-field mode. Images were processed and analyzed using Pannoramic Viewer (version 1.15.4, 3D Histech, Hungary), with manual segmentation of cell infiltration performed using ImageJ software (version 1.51, National Institutes of Health, Bethesda, MD, USA). Cell infiltration was calculated as the relative area of lung parenchyma where visible alveolar thickening and formation of granulomas occurred. Granuloma size accounted for the area of the manually segmented features. At least 3 mice were analyzed in each condition and time point.

Raman Mapping of Lungs. Snap-frozen lungs embedded in OCT compound were cryo-sectioned and gently rinsed with PBS 1×, Milli-Q water, and methanol, in order to remove any excess OCT compound. Sections were then dried at 37 °C before imaging under a DXRxi Raman microscope (Thermo Scientific, UK), with a 50× objective. Raman maps were obtained using a 633 nm laser operating at 0.4 mW, through a 50 μm pinhole aperture with an exposure time of 0.125 s. Correlation maps were calculated using the OMNICxi software (Thermo Scientific, UK), after comparing to a reference spectrum of GO sample (Figure S21).

Statistical Analysis. Every experiment was repeated at least twice with triplicates or sextuplicates for each condition. Data are represented as mean ± SD and were statistically analyzed with IBM SPSS software (version 22) or GraphPad Prism (version 6.05) using analysis of variance (one-way or two-way ANOVA) with $p < 0.05$ considered significant. *In vivo* data were analyzed in GraphPad Prism using the Kruskal−Wallis test with *post hoc* Dunn's multiple comparisons test with $p < 0.05$ considered significant.

ASSOCIATED CONTENT

Ⓢ Supporting Information

The Supporting Information is available free of charge on the ACS Publications website at DOI: 10.1021/acsnano.7b07734.

> Table S1: Characterization of GO in the cell culture medium; Supporting Figures S1−S21 (PDF)
> Confocal live imaging of untreated BEAS-2B cells (AVI)
> Confocal live imaging of BEAS-2B cells treated with s-GO in the absence of FBS (AVI)
> Confocal live imaging of BEAS-2B cells treated with l-GO in the absence of FBS (AVI)
> Confocal live imaging of BEAS-2B cells (AVI)
> Confocal live imaging of BEAS-2B cells treated with s-GO in the absence of FBS (AVI)
> Confocal live imaging of BEAS-2B cells treated with l-GO in the absence of FBS (AVI)
> Confocal live imaging of untreated BEAS-2B cells (AVI)
> Confocal live imaging of BEAS-2B cells treated with s-GO in the presence of FBS (AVI)
> Confocal live imaging of BEAS-2B cells treated with l-GO in the presence of FBS (AVI)
> Confocal live imaging of untreated BEAS-2B cells (AVI)
> Confocal live imaging of BEAS-2B cells treated with s-GO in the presence of FBS (AVI)
> Confocal live imaging of BEAS-2B cells treated with l-GO in the presence of FBS (AVI)

AUTHOR INFORMATION

Corresponding Authors
*E-mail: cyrill.bussy@manchester.ac.uk.
*E-mail: kostas.kostarelos@manchester.ac.uk.

ORCID Ⓞ
Artur Filipe Rodrigues: 0000-0002-4078-3455
Cyrill Bussy: 0000-0001-8870-443X
Kostas Kostarelos: 0000-0002-2224-6672

Author Contributions

[#]S. Vranic and A. F. Rodrigues contributed equally to this study.

Notes

The authors declare no competing financial interest.

REFERENCES

(1) Wick, P.; Louw-Gaume, A. E.; Kucki, M.; Krug, H. F.; Kostarelos, K.; Fadeel, B.; Dawson, K. A.; Salvati, A.; Vazquez, E.; Ballerini, L.; Tretiach, M.; Benfenati, F.; Flahaut, E.; Gauthier, L.; Prato, M.; Bianco, A. Classification Framework for Graphene-Based Materials. *Angew. Chem., Int. Ed.* **2014**, *53*, 7714−7718.

(2) Kostarelos, K.; Novoselov, K. S. Exploring the Interface of Graphene and Biology. *Science* **2014**, *344*, 261−263.

(3) Zurutuza, A.; Marinelli, C. Challenges and Opportunities in Graphene Commercialization. *Nat. Nanotechnol.* **2014**, *9*, 730−734.

(4) Ferrari, A. C.; Bonaccorso, F.; Fal'ko, V.; Novoselov, K. S.; Roche, S.; Boggild, P.; Borini, S.; Koppens, F. H.; Palermo, V.; Pugno, N.; Garrido, J. A.; Sordan, R.; Bianco, A.; Ballerini, L.; Prato, M.; Lidorikis, E.; Kivioja, J.; Marinelli, C.; Ryhänen, T.; et al. Science and Technology Roadmap for Graphene, Related Two-Dimensional Crystals, and Hybrid Systems. *Nanoscale* **2015**, *7*, 4598−4810.

(5) Wang, X.; Duch, M. C.; Mansukhani, N.; Ji, Z.; Liao, Y. P.; Wang, M.; Zhang, H.; Sun, B.; Chang, C. H.; Li, R.; Meng, H.; Xia, T.; Hersam, T. C.; Nel, A. E. Use of a Pro-Fibrogenic Mechanism-Based Predictive Toxicological Approach for Tiered Testing and Decision Analysis of Carbonaceous Nanomaterials. *ACS Nano* **2015**, *9*, 3032−3043.

(6) Ma-Hock, L.; Strauss, V.; Treumann, S.; Kuttler, K.; Wohlleben, W.; Hofmann, T.; Groters, S.; Wiench, K.; van Ravenzwaay, B.; Landsiedel, R. Comparative Inhalation Toxicity of Multi-Wall Carbon Nanotubes, Graphene, Graphite Nanoplatelets and Low Surface Carbon Black. *Part. Fibre Toxicol.* **2013**, *10*, 23.

(7) Bhattacharya, K.; Mukherjee, S. P.; Gallud, A.; Burkert, S. C.; Bistarelli, S.; Bellucci, S.; Bottini, M.; Star, A.; Fadeel, B. Biological Interactions of Carbon-Based Nanomaterials: From Coronation to Degradation. *Nanomedicine* **2016**, *12*, 333−351.

(8) Nel, A.; Xia, T.; Mädler, L.; Li, N. Toxic Potential of Materials at the Nanolevel. *Science* **2006**, *311*, 622−627.

(9) Nel, A. E.; Mädler, L.; Velegol, D.; Xia, T.; Hoek, E. M.; Somasundaran, P.; Klaessig, F.; Castranova, V.; Thompson, M. Understanding Biophysicochemical Interactions at the Nano-Bio Interface. *Nat. Mater.* **2009**, *8*, 543−557.

(10) Xia, T.; Kovochich, M.; Brant, J.; Hotze, M.; Sempf, J.; Oberley, T.; Sioutas, C.; Yeh, J. I.; Wiesner, M. R.; Nel, A. E. Comparison of the Abilities of Ambient and Manufactured Nanoparticles to Induce Cellular Toxicity According to an Oxidative Stress Paradigm. *Nano Lett.* **2006**, *6*, 1794−1807.

(11) Yue, H.; Wei, W.; Yue, Z.; Wang, B.; Luo, N.; Gao, Y.; Ma, D.; Ma, G.; Su, Z. The Role of the Lateral Dimension of Graphene Oxide in the Regulation of Cellular Responses. *Biomaterials* **2012**, *33*, 4013−4021.

(12) Ma, J.; Liu, R.; Wang, X.; Liu, Q.; Chen, Y.; Valle, R. P.; Zuo, Y. Y.; Xia, T.; Liu, S. Crucial Role of Lateral Size for Graphene Oxide in Activating Macrophages and Stimulating Pro-Inflammatory Responses in Cells and Animals. *ACS Nano* **2015**, *9*, 10498−10515.

(13) Orecchioni, M.; Jasim, D. A.; Pescatori, M.; Manetti, R.; Fozza, C.; Sgarrella, F.; Bedognetti, D.; Bianco, A.; Kostarelos, K.; Delogu, L. G. Molecular and Genomic Impact of Large and Small Lateral Dimension Graphene Oxide Sheets on Human Immune Cells from Healthy Donors. *Adv. Healthcare Mater.* **2016**, *5*, 276−287.

(14) Li, Y.; Feng, L.; Shi, X.; Wang, X.; Yang, Y.; Yang, K.; Liu, T.; Yang, G.; Liu, Z. Surface Coating-Dependent Cytotoxicity and Degradation of Graphene Derivatives: Towards the Design of Non-Toxic, Degradable Nano-Graphene. *Small* **2014**, *10*, 1544−1554.

(15) Chong, Y.; Ge, C.; Yang, Z.; Garate, J. A.; Gu, Z.; Weber, J. K.; Liu, J.; Zhou, R. Reduced Cytotoxicity of Graphene Nanosheets Mediated by Blood-Protein Coating. *ACS Nano* **2015**, *9*, 5713−5724.

(16) Duan, G.; Kang, S. G.; Tian, X.; Garate, J. A.; Zhao, L.; Ge, C.; Zhou, R. Protein Corona Mitigates the Cytotoxicity of Graphene Oxide by Reducing Its Physical Interaction with Cell Membrane. *Nanoscale* **2015**, *7*, 15214−15224.

(17) Hu, W.; Peng, C.; Lv, M.; Li, X.; Zhang, Y.; Chen, N.; Fan, C.; Huang, Q. Protein Corona-Mediated Mitigation of Cytotoxicity of Graphene Oxide. *ACS Nano* **2011**, *5*, 3693−3700.

(18) Chatterjee, N.; Yang, J. S.; Park, K.; Oh, S. M.; Park, J.; Choi, J. Screening of Toxic Potential of Graphene Family Nanomaterials Using *in Vitro* and Alternative *in Vivo* Toxicity Testing Systems. *Environ. Health Toxicol.* **2015**, *30*, e2015007.

(19) Bussy, C.; Ali-Boucetta, H.; Kostarelos, K. Safety Considerations for Graphene: Lessons Learnt from Carbon Nanotubes. *Acc. Chem. Res.* **2013**, *46*, 692−701.

(20) Rauti, R.; Lozano, N.; León, V.; Scaini, D.; Musto, M.; Rago, I.; Ulloa Severino, F. P.; Fabbro, A.; Casalis, L.; Vázquez, E.; Kostarelos, K.; Prato, M.; Ballerini, L. Graphene Oxide Nanosheets Reshape Synaptic Function in Cultured Brain Networks. *ACS Nano* **2016**, *10*, 4459−4471.

(21) Mukherjee, S. P.; Lozano, N.; Kucki, M.; Del Rio-Castillo, A. E.; Newman, L.; Vázquez, E.; Kostarelos, K.; Wick, P.; Fadeel, B. Detection of Endotoxin Contamination of Graphene Based Materials Using the TNF-A Expression Test and Guidelines for Endotoxin-Free Graphene Oxide Production. *PLoS One* **2016**, *11*, e0166816.

(22) Jasim, D.; Lozano, N.; Kostarelos, K. Synthesis of Few-Layered, High-Purity Graphene Oxide Sheets from Different Graphite Sources for Biology. *2D Mater.* **2016**, *3*, 014006.

(23) Dresselhaus, M. S.; Dresselhaus, G.; Jorio, A.; Souza Filho, A. G.; Pimenta, M. A.; Saito, R. Single Nanotube Raman Spectroscopy. *Acc. Chem. Res.* 2002, *35*, 1070−1078.

(24) Kostarelos, K.; Novoselov, K. S. Graphene Devices for Life. *Nat. Nanotechnol.* 2014, *9*, 744−745.

(25) Gosens, I.; Post, J. A.; de la Fonteyne, L. J.; Jansen, E. H.; Geus, J. W.; Cassee, F. R.; de Jong, W. H. Impact of Agglomeration State of Nano- and Submicron Sized Gold Particles on Pulmonary Inflammation. *Part. Fibre Toxicol.* 2010, *7*, 37.

(26) Jiang, Y.; Raliya, R.; Fortner, J. D.; Biswas, P. Graphene Oxides in Water: Correlating Morphology and Surface Chemistry with Aggregation Behavior. *Environ. Sci. Technol.* 2016, *50*, 6964−6973.

(27) Shih, C. J.; Lin, S.; Sharma, R.; Strano, M. S.; Blankschtein, D. Understanding the pH-Dependent Behavior of Graphene Oxide Aqueous Solutions: A Comparative Experimental and Molecular Dynamics Simulation Study. *Langmuir* 2012, *28*, 235−241.

(28) Vranic, S.; Gosens, I.; Jacobsen, N. R.; Jensen, K. A.; Bokkers, B.; Kermanizadeh, A.; Stone, V.; Baeza-Squiban, A.; Cassee, F. R.; Tran, L.; Boland, S. Impact of Serum as a Dispersion Agent for *in Vitro* and *in Vivo* Toxicological Assessments of TiO2 Nanoparticles. *Arch. Toxicol.* 2017, *91*, 353−363.

(29) Lesniak, A.; Fenaroli, F.; Monopoli, M. P.; Åberg, C.; Dawson, K. A.; Salvati, A. Effects of the Presence or Absence of a Protein Corona on Silica Nanoparticle Uptake and Impact on Cells. *ACS Nano* 2012, *6*, 5845−5857.

(30) Kapralov, A. A.; Feng, W. H.; Amoscato, A. A.; Yanamala, N.; Balasubramanian, K.; Winnica, D. E.; Kisin, E. R.; Kotchey, G. P.; Gou, P.; Sparvero, L. J.; Ray, P.; Mallampalli, R. K.; Klein-Seetharaman, J.; Fadeel, B.; Star, A.; Shvedova, A. A.; Kagan, V. E. Adsorption of Surfactant Lipids by Single-Walled Carbon Nanotubes in Mouse Lung Upon Pharyngeal Aspiration. *ACS Nano* 2012, *6*, 4147−4156.

(31) Shang, J.; Ma, L.; Li, J.; Ai, W.; Yu, T.; Gurzadyan, G. G. The Origin of Fluorescence from Graphene Oxide. *Sci. Rep.* 2012, *2*, 792.

(32) Vempati, S.; Uyar, T. Fluorescence from Graphene Oxide and the Influence of Ionic, Π-Π Interactions and Heterointerfaces: Electron or Energy Transfer Dynamics. *Phys. Chem. Chem. Phys.* 2014, *16*, 21183−21203.

(33) Ali-Boucetta, H.; Al-Jamal, K. T.; Kostarelos, K. Cytotoxic Assessment of Carbon Nanotube Interaction with Cell Cultures. *Methods Mol. Biol.* 2011, *726*, 299−312.

(34) Liao, K. H.; Lin, Y. S.; Macosko, C. W.; Haynes, C. L. Cytotoxicity of Graphene Oxide and Graphene in Human Erythrocytes and Skin Fibroblasts. *ACS Appl. Mater. Interfaces* 2011, *3*, 2607−2615.

(35) Al-Jamal, K. T.; Kostarelos, K. Assessment of Cellular Uptake and Cytotoxicity of Carbon Nanotubes Using Flow Cytometry. *Methods Mol. Biol.* 2010, *625*, 123−134.

(36) Vranic, S.; Kostarelos, K. High-Accuracy Determination of Cytotoxic Responses from Graphene Oxide Exposure Using Imaging Flow Cytometry. *Methods Mol. Biol.* 2017, *1570*, 287−300.

(37) Marangon, I.; Boggetto, N.; Ménard-Moyon, C.; Venturelli, E.; Béoutis, M. L.; Péchoux, C.; Luciani, N.; Wilhelm, C.; Bianco, A.; Gazeau, F. Intercellular Carbon Nanotube Translocation Assessed by Flow Cytometry Imaging. *Nano Lett.* 2012, *12*, 4830−4837.

(38) Saptarshi, S. R.; Duschl, A.; Lopata, A. L. Interaction of Nanoparticles with Proteins: Relation to Bio-Reactivity of the Nanoparticle. *J. Nanobiotechnol.* 2013, *11*, 26.

(39) Seabra, A. B.; Paula, A. J.; de Lima, R.; Alves, O. L.; Durán, N. Nanotoxicity of Graphene and Graphene Oxide. *Chem. Res. Toxicol.* 2014, *27*, 159−168.

(40) Gurunathan, S.; Han, J. W.; Dayem, A. A.; Eppakayala, V.; Kim, J. H. Oxidative Stress-Mediated Antibacterial Activity of Graphene Oxide and Reduced Graphene Oxide in Pseudomonas Aeruginosa. *Int. J. Nanomed.* 2012, *7*, 5901−5914.

(41) Chang, Y.; Yang, S. T.; Liu, J. H.; Dong, E.; Wang, Y.; Cao, A.; Liu, Y.; Wang, H. *In Vitro* Toxicity Evaluation of Graphene Oxide on A549 Cells. *Toxicol. Lett.* 2011, *200*, 201−210.

(42) Kucki, M.; Rupper, P.; Sarrieu, C.; Melucci, M.; Treossi, E.; Schwarz, A.; León, V.; Kraegeloh, A.; Flahaut, E.; Vázquez, E.;

(43) Palermo, V.; Wick, P. Interaction of Graphene-Related Materials with Human Intestinal Cells: An *In Vitro* Approach. *Nanoscale* 2016, *8*, 8749−8760.

(43) Zhang, Y.; Ali, S. F.; Dervishi, E.; Xu, Y.; Li, Z.; Casciano, D.; Biris, A. S. Cytotoxicity Effects of Graphene and Single-Wall Carbon Nanotubes in Neural Phaeochromocytoma-Derived PC12 Cells. *ACS Nano* 2010, *4*, 3181−3186.

(44) Sanchez, V. C.; Jachak, A.; Hurt, R. H.; Kane, A. B. Biological Interactions of Graphene-Family Nanomaterials: An Interdisciplinary Review. *Chem. Res. Toxicol.* 2012, *25*, 15−34.

(45) Zhang, P.; Yin, H.; Wang, S.; Wei, Y.; Peng, N.; Bi, W.; Wang, X. Different Effects of H2O2 Treatment on Cervical Squamous Carcinoma Cells and Adenocarcinoma Cells. *Arch. Med. Sci.* 2015, *11*, 1308−1313.

(46) Vranic, S.; Garcia-Verdugo, I.; Darnis, C.; Sallenave, J. M.; Boggetto, N.; Marano, F.; Boland, S.; Baeza-Squiban, A. Internalization of SiO2 Nanoparticles by Alveolar Macrophages and Lung Epithelial Cells and Its Modulation by the Lung Surfactant Substitute Curosurf. *Environ. Sci. Pollut. Res.* 2013, *20*, 2761−2770.

(47) Kienast, K.; Knorst, M.; Müller-Quernheim, J.; Ferlinz, R. Modulation of IL-1 Beta, IL-6, IL-8, TNF-Alpha, and TGF-Beta Secretions by Alveolar Macrophages under NO2 Exposure. *Lung* 1996, *174*, 57−67.

(48) Qu, G.; Liu, S.; Zhang, S.; Wang, L.; Wang, X.; Sun, B.; Yin, N.; Gao, X.; Xia, T.; Chen, J. J.; Jiang, G. B. Graphene Oxide Induces Toll-Like Receptor 4 (TLR4)-Dependent Necrosis in Macrophages. *ACS Nano* 2013, *7*, 5732−5745.

(49) Guadagnini, R.; Kenzaoui, B. H.; Walker, L.; Pojana, G.; Magdolenova, Z.; Bilanicova, D.; Saunders, M.; Juillerat-Jeanneret, L.; Marcomini, A.; Huk, A.; Dusinska, M.; Fjellsbø, L. M.; Marano, F.; Boland, S. Toxicity Screenings of Nanomaterials: Challenges Due to Interference with Assay Processes and Components of Classic *in Vitro* Tests. *Nanotoxicology* 2015, *9*, 13−24.

(50) Kroll, A.; Pillukat, M. H.; Hahn, D.; Schnekenburger, J. Interference of Engineered Nanoparticles with *In Vitro* Toxicity Assays. *Arch. Toxicol.* 2012, *86*, 1123−1136.

(51) Stumpo, D. J.; Lai, W. S.; Blackshear, P. J. Inflammation: Cytokines and RNA-Based Regulation. *WIRES RNA* 2010, *1*, 60−80.

(52) Chandel, N. S.; Schumacker, P. T.; Arch, R. H. Reactive Oxygen Species Are Downstream Products of TRAF-Mediated Signal Transduction. *J. Biol. Chem.* 2001, *276*, 42728−42736.

(53) Veranth, J. M.; Reilly, C. A.; Veranth, M. M.; Moss, T. A.; Langelier, C. R.; Lanza, D. L.; Yost, G. S. Inflammatory Cytokines and Cell Death in BEAS-2B Lung Cells Treated with Soil Dust, Lipopolysaccharide, and Surface-Modified Particles. *Toxicol. Sci.* 2004, *82*, 88−96.

(54) Li, Q.; Engelhardt, J. F. Interleukin-1Beta Induction of NFKappaB Is Partially Regulated by H2O2-Mediated Activation of NFKappaB-Inducing Kinase. *J. Biol. Chem.* 2006, *281*, 1495−1505.

(55) Dinarello, C. A. Immunological and Inflammatory Functions of the Interleukin-1 Family. *Annu. Rev. Immunol.* 2009, *27*, 519−550.

(56) Yang, L.; Zhang, R.; Liu, B.; Wang, J.; Wang, S.; Han, M. Y.; Zhang, Z. Π-Conjugated Carbon Radicals at Graphene Oxide to Initiate Ultrastrong Chemiluminescence. *Angew. Chem., Int. Ed.* 2014, *53*, 10109−10113.

(57) Li, R.; Mansukhani, N. D.; Guiney, L. M.; Ji, Z.; Zhao, Y.; Chang, C. H.; French, C. T.; Miller, J. F.; Hersam, M. C.; Nel, A. E.; Xia, T. Identification and Optimization of Carbon Radicals on Hydrated Graphene Oxide for Ubiquitous Antibacterial Coatings. *ACS Nano* 2016, *10*, 10966−10980.

(58) Tian, X.; Yang, Z.; Duan, G.; Wu, A.; Gu, Z.; Zhang, L.; Chen, C.; Chai, Z.; Ge, C.; Zhou, R. Graphene Oxide Nanosheets Retard Cellular Migration *Via* Disruption of Actin Cytoskeleton. *Small* 2017, *13*, 1602133.

(59) Li, Y.; Yuan, H.; von dem Bussche, A.; Creighton, M.; Hurt, R. H.; Kane, A. B.; Gao, H. Graphene Microsheets Enter Cells through Spontaneous Membrane Penetration at Edge Asperities and Corner Sites. *Proc. Natl. Acad. Sci. U. S. A.* 2013, *110*, 12295−12300.

(60) Houle, F.; Rousseau, S.; Morrice, N.; Luc, M.; Mongrain, S.; Turner, C. E.; Tanaka, S.; Moreau, P.; Huot, J. Extracellular Signal-Regulated Kinase Mediates Phosphorylation of Tropomyosin-1 to Promote Cytoskeleton Remodeling in Response to Oxidative Stress: Impact on Membrane Blebbing. *Mol. Biol. Cell* **2003**, *14*, 1418−1432.

(61) Poland, C. A.; Duffin, R.; Kinloch, I.; Maynard, A.; Wallace, W. A.; Seaton, A.; Stone, V.; Brown, S.; Macnee, W.; Donaldson, K. Carbon Nanotubes Introduced into the Abdominal Cavity of Mice Show Asbestos-Like Pathogenicity in a Pilot Study. *Nat. Nanotechnol.* **2008**, *3*, 423−428.

(62) Schinwald, A.; Murphy, F. A.; Jones, A.; MacNee, W.; Donaldson, K. Graphene-Based Nanoplatelets: A New Risk to the Respiratory System as a Consequence of Their Unusual Aerodynamic Properties. *ACS Nano* **2012**, *6*, 736−746.

(63) Jasim, D. A.; Murphy, S.; Newman, L.; Mironov, A.; Prestat, E.; McCaffrey, J.; Ménard-Moyon, C.; Rodrigues, A. F.; Bianco, A.; Haigh, S.; Lennon, R.; Kostarelos, K. The Effects of Extensive Glomerular Filtration of Thin Graphene Oxide Sheets on Kidney Physiology. *ACS Nano* **2016**, *10*, 10753−10767.

(64) Ali-Boucetta, H.; Bitounis, D.; Raveendran-Nair, R.; Servant, A.; Van den Bossche, J.; Kostarelos, K. Purified Graphene Oxide Dispersions Lack *in Vitro* Cytotoxicity and *in Vivo* Pathogenicity. *Adv. Healthcare Mater.* **2013**, *2*, 433−441.

(65) Anderson, J. M.; Rodriguez, A.; Chang, D. T. Foreign Body Reaction to Biomaterials. *Semin. Immunol.* **2008**, *20*, 86−100.

(66) Herzog, E.; Byrne, H. J.; Davoren, M.; Casey, A.; Duschl, A.; Oostingh, G. J. Dispersion Medium Modulates Oxidative Stress Response of Human Lung Epithelial Cells Upon Exposure to Carbon Nanomaterial Samples. *Toxicol. Appl. Pharmacol.* **2009**, *236*, 276−281.

(67) Zhao, J.; Wang, Z.; White, J. C.; Xing, B. Graphene in the Aquatic Environment: Adsorption, Dispersion, Toxicity and Transformation. *Environ. Sci. Technol.* **2014**, *48*, 9995−10009.

(68) Schweitzer, K. S.; Hatoum, H.; Brown, M. B.; Gupta, M.; Justice, M. J.; Beteck, B.; Van Demark, M.; Gu, Y.; Presson, R. G.; Hubbard, W. C.; Petrache, I. Mechanisms of Lung Endothelial Barrier Disruption Induced by Cigarette Smoke: Role of Oxidative Stress and Ceramides. *Am. J. Physiol Lung Cell Mol. Physiol.* **2011**, *301*, L836−L846.

(69) Németh, Z. H.; Deitch, E. A.; Davidson, M. T.; Szabó, C.; Vizi, E. S.; Haskó, G. Disruption of the Actin Cytoskeleton Results in Nuclear Factor-KappaB Activation and Inflammatory Mediator Production in Cultured Human Intestinal Epithelial Cells. *J. Cell. Physiol.* **2004**, *200*, 71−81.

(70) Lee, J. K.; Jeong, A. Y.; Bae, J.; Seok, J. H.; Yang, J. Y.; Roh, H. S.; Jeong, J.; Han, Y.; Jeong, J.; Cho, W. S. The Role of Surface Functionalization on the Pulmonary Inflammogenicity and Translocation into Mediastinal Lymph Nodes of Graphene Nanoplatelets in Rats. *Arch. Toxicol.* **2017**, *91*, 667−676.